Utah State University

DigitalCommons@USU

All Graduate Theses and Dissertations | Graduate Studies

5-2011

Automatic Particle Image Velocimetry Uncertainty Quantification

Benjamin H. Timmins
Utah State University

Follow this and additional works at: https://digitalcommons.usu.edu/etd

Part of the Mechanical Engineering Commons

Recommended Citation

Timmins, Benjamin H., "Automatic Particle Image Velocimetry Uncertainty Quantification" (2011). *All Graduate Theses and Dissertations*. 884.
https://digitalcommons.usu.edu/etd/884

This Thesis is brought to you for free and open access by the Graduate Studies at DigitalCommons@USU. It has been accepted for inclusion in All Graduate Theses and Dissertations by an authorized administrator of DigitalCommons@USU. For more information, please contact digitalcommons@usu.edu.

AUTOMATIC PARTICLE IMAGE VELOCIMETRY UNCERTAINTY QUANTIFICATION

by

Benjamin H. Timmins

A thesis submitted in partial fulfillment
of the requirements for the degree

of

MASTER OF SCIENCE

in

Mechanical Engineering

Approved:

Dr. Barton L. Smith Major Professor	Dr. Robert E. Spall Committee Member
Dr. Heng Ban Committee Member	Dr. Byron R. Burnham Dean of Graduate Studies

UTAH STATE UNIVERSITY
Logan, Utah

2011

Copyright © Benjamin H. Timmins 2011

All Rights Reserved

Abstract

Automatic Particle Image Velocimetry Uncertainty Quantification

by

Benjamin H. Timmins, Master of Science

Utah State University, 2011

Major Professor: Dr. Barton L. Smith
Department: Mechanical and Aerospace Engineering

The uncertainty of any measurement is the interval in which one believes the actual error lies. Particle Image Velocimetry (PIV) measurement error depends on the PIV algorithm used, a wide range of user inputs, flow characteristics, and the experimental setup. Since these factors vary in time and space, they lead to nonuniform error throughout the flow field. As such, a universal PIV uncertainty estimate is not adequate and can be misleading. This is of particular interest when PIV data are used for comparison with computational or experimental data.

A method to estimate the uncertainty due to the PIV calculation of each individual velocity measurement is presented. The relationship between four error sources and their contribution to PIV error is first determined. The sources, or parameters, considered are particle image diameter, particle density, particle displacement, and velocity gradient, although this choice in parameters is arbitrary and may not be complete. This information provides a four-dimensional "uncertainty surface" for the PIV algorithm used. After PIV processing, our code "measures" the value of each of these parameters and estimates the velocity uncertainty for each vector in the flow field. The reliability of the methodology is validated using known flow fields so the actual error can be determined. Analysis shows that,

for most flows, the uncertainty distribution obtained using this method fits the confidence interval. The method is general and can be adapted to any PIV analysis.

(82 pages)

To my supportive parents Garth and Sarah, and my wife Karianne.

Acknowledgments

This work would not have been possible without the help of my advisor Dr. Barton L. Smith, Dr. Pavlos V. Vlachos of Virginia Tech, and Dr. Nam Dinh of Idaho National Laboratory. This work has been supported by the United States Department of Energy through the Idaho National Laboratory's LDRD Project NE-156. Special thanks to John Charonko for providing PRANA, the PIV algorithm used, Satyapraksh Karri for his help with the robust gradient estimation method, Kyle Horne for programming help and the use of his cluster, and Katie Mabey for her constant support and document preparation help.

Benjamin H. Timmins

Contents

Page

Abstract . . . . . **iii**

Acknowledgments . . . . . **vi**

List of Tables . . . . . **viii**

List of Figures . . . . . **ix**

1 Problem Statement **1**

2 Literature Review **3**
- 2.1 Particle Image Velocimetry 3
- 2.2 PIV Algorithms 4
- 2.3 Sources of Uncertainty in PIV 10
  - 2.3.1 Outlier Error 10
  - 2.3.2 Bias Error 12
  - 2.3.3 Precision Error 16

3 Objectives **19**

4 Procedures **20**
- 4.1 PIV Algorithms 20
- 4.2 Uncertainty Estimates for Specific PIV Algorithms 21
- 4.3 Uncertainty Estimation 22
  - 4.3.1 Synthetic Images 23
  - 4.3.2 Generating the Uncertainty Surface 30
  - 4.3.3 Computational Cost 34
- 4.4 Uncertainty Comparison 36
- 4.5 Image Parameter Quantification 37

5 Results **45**
- 5.1 Assessing the Appropriateness of the Uncertainty Band 45
- 5.2 Uncertainty Field Computations Compared with Error 46
- 5.3 Correction of Uncertainty Estimates 54
  - 5.3.1 Implementation of an Uncertainty Floor 56
  - 5.3.2 Burger Vortex Investigation 58

6 Conclusion **67**

References **69**

List of Tables

Table Page

4.1 Range of the Computed Uncertainty Estimates 33

4.2 PIV Processing Parameters Used to Compute the Uncertainty Surface . . . 33

5.1 Uncertainty Effectiveness ($u - U_r^- < u_{true} < u + U_r^+$) for Both the u and v Velocity Components 46

5.2 Uncertainty Effectiveness after a Floor of 0.050 Pixels for the SCC Method, and 0.023 Pixels for the RPC Method Was Used 58

List of Figures

Figure Page

2.1 Plot of the computational time order of magnitude against the interrogation window size (N). This plot assumes that the interrogation regions are square ($N \times N$). 5

2.2 A correlation map $C(r, s)$ example which can be calculated from either Eqn. 2.1 or Eqn. 2.2. 6

2.3 The cross correlation function $C(r, s)$ of: (a) a weak cross correlation with multiple peaks and high amplitude background noise and, (b) a weak cross correlation with a single peak and high magnitude ridge. 11

2.4 PIV velocity over time (a) for low frequency sinusoidal turbulent velocity fluctuations data with high frequency sinusoidal noise and, (b) constant laminar velocity data with high frequency sinusoidal noise. 17

4.1 Average subpixel displacement error as computed by DaVis 7.2.2 and PRANA for different diameters, d_τ, at a particle image density of 0.0293 particles/pixel^2. 22

4.2 Volume showing particles and gaussian laser sheet profile [1]. 24

4.3 Two images of the same space as shown as particles move through a volume. It is illustrated that the volume containing particles needs to be larger than the images desired. 25

4.4 A syntectic image that is 256×256 pixels with 3 pixel diameter gaussian particles, and a 1mm thick light sheet. 26

4.5 Combined Couette-Poiseuille flow velocity profiles for varying pressure gradients. 28

4.6 Normalized histogram of background noise from PCO sensicam QE CCD and Photron FastCam APX RS CMOS cameras. 30

4.7 Theoretical histogram showing the distribution of computed displacements and the true displacement D_{true}. r_{ave} is the average displacement that is calculated by the PIV algorithm. The value b_k is the systematic uncertainty value. r_{low} and r_{high} are the upper and lower bounds in which 95% of the data are contained. 31

4.8 Values of U_r^- and U_r^+ for different numbers of samples used to compute them. 34

4.9 U_r^+ contours as a function of particle image diameter and seeding density for no gradient and 0.8 pixel uniform displacement for the SCC method. The contour increment is 0.002 pixels. 35

4.10 U_r^+ contours as a function of displacement and gradient for 2.50 pixel particle image diameter and 0.0195 particle/pixel^2 density. The contour increment is 0.10 pixels. 35

4.11 A comparison between the rms uncertainty reported by Raffel and the bias, upper random and lower random uncertainty from this study due to particle image diameter. The SCC method is used with interrogation regions of 16×16 pixels with $N_I = 5$. All images have 8 bit resolution, no noise, and particle image diameters of 2.0 pixels. 37

4.12 A comparison between the rms uncertainty reported by Raffel and the bias, upper random and lower random uncertainty from this study due to displacement. The SCC method is used with interrogation regions of 32×32 pixels with $N_I = 10.2$. All images have 8 bit resolution, no noise, and particle image diameters of 2.2 pixels. 38

4.13 A comparison between the rms uncertainty reported by Raffel and the bias, upper random and lower random uncertainty from this study due to shear. The SCC method is used with interrogation regions of 16×16 pixels with $N_I = 5$. All images have 8 bit resolution, no noise, and particle image diameters of 2.0 pixels. 39

4.14 A singe row added to the preceding and following rows of pixel intensity. Based on this singe row the algorithm computed the particle image diameter such that the relative error $[\mathrm{abs}(\mathrm{d}_{\tau\mathrm{true}} - \mathrm{d}_\tau)/\mathrm{d}_{\tau\mathrm{true}}]100\% = 3.7\%$. The particle image density relative error was computed the same way to be 8.8%. 39

4.15 Particle image diameter, d_τ, is estimated with varying number of rows sampled. The noise threshold is set to 10%, 30%, and 50% of the maximum intensity. 40

4.16 Particle image size algorithm results as a function of particle size. 41

4.17 A section of an image with particle image diameters of 2.5 pixels, density 0.0192 particles/pixel^2 and (a) 0.0% background noise, (b) 10.0% background noise, (c) and 20.0% background noise. 43

4.18 The effect of image background noise on the estimated particle image diameter. The actual value is 2.5 pixels. Uncertainty band width is computed from a Student's t distribution of 4 samples and a 95% confidence interval. 44

4.19 The effect of image background noise on the estimated particle image density. The actual value is 0.02. Uncertainty band width is computed from a Student's t distribution of 4 samples a 95% confidence interval. 44

5.1 Plot of the calculated displacement of the uniform profile velocity field with no background noise computed with the RPC method. 47

5.2 Plot of the width of the uncertainty bar associated with each displacement vector and superimposed error contour for the uniform flow case. The error level contours are 0.0, 0.05, and 0.1 pixels. 48

5.3 Plot of the calculated displacement of the linear profile velocity field with no background noise as computed with the RPC method. 48

5.4 Plot of the width of the uncertainty bar associated with each displacement vector and superimposed error contour for the linear profile case. The error level contours are set at 0.0, 0.1, and 0.2 pixels. 49

5.5 Plot of the calculated Couette-Poiseuille flow field displacement with no background noise as computed by the RPC method. 50

5.6 Plot of the width of the uncertainty bar associated with each displacement vector and superimposed error contour for the Couette-Poiseuille flow case. The error level contours are 0.0, 0.1, and 0.2 pixels. 50

5.7 Comparison of the computed value of u and its 95% uncertainty bar at constant $x = 31$mm for a Couette-Poiseuille flow which has 10% background noise. 51

5.8 Plot of the calculated Burger's Vortex flow field displacement with no background noise as computed by the RPC method. 51

5.9 Plot of the width of the uncertainty bar associated with each displacement vector and superimposed error contour for the Burger Vortex case. The error level contours are 0.0, 0.1, and 0.2 pixels. 52

5.10 Plot of the PIV Challenge 2005 case B flow field displacement as computed by the RPC method. 52

5.11 Plot of the width of the uncertainty bar associated with each displacement vector in the DNS flow field with superimposed error contours. The error level contours are set at 0.0, 0.1, 0.2, and 0.3 pixels. 53

5.12 A plot of the local uncertainty estimate as a percentage of local velocity for the combined Couette-Poiseuille flow. 54

5.13 A plot of the local uncertainty estimate as a percentage of local velocity for PIV Challenge 2005 case B flow field. 55

5.14 The computed standard deviation of the y velocity component for varying x velocity component particle image displacement for both the standard cross correlation and robust phase correlation methods. 55

5.15 The computed standard deviation of the y velocity component for varying x velocity component particle image subpixel pixel displacements. 56

5.16 The effects of a floor minimum uncertainty value for the uniform flow, linear profile, Couette-Poiseuille, and Burger's vortex flows when processed with the SCC method. 57

5.17 Uncertainty effectiveness shown as a function of the floor value for three Burger vortex cases, each with different strengths. 59

5.18 u velocity locations where the true value is not contained within the uncertainty bounds. 59

5.19 v velocity locations where the true value is not contained within the uncertainty bounds. 60

5.20 Velocity field of the Rankine vortex. 61

5.21 Flood contour of the subpixel displacement estimates for the u velocity component of the Burger vortex case. Line contours are overlaid showing regions where the true value was not captured by computed uncertainty bounds. . . 62

5.22 Flood contour of the subpixel displacement estimates for the v velocity component of the Burger vortex case. Line contours are overlaid showing regions where the true value was not captured by computed uncertainty bounds. . . 63

5.23 Flood contour of the subpixel displacement estimates for the u velocity component of the Rankine vortex case. Line contours are overlaid showing regions where the true value was not captured by computed uncertainty bounds. . . 63

5.24 Flood contour of the subpixel displacement estimates for the v velocity component of the Rankine vortex case. Line contours are overlaid showing regions where the true value was not captured by computed uncertainty bounds. . . 64

5.25 Individual C_f values computed for different shear levels and orthogonal velocity component displacement magnitudes. A linear curve fit is applied to the data which can be used to compute a correction factor for two-dimensional flows. 65

5.26 Uncertainty effectiveness shown as a function of the floor value for the high strength Burger vortex case. Both the original results and the corrected results using the uncertainty scaling based on the orthogonal velocity component magnitude are shown. 66

Chapter 1

Problem Statement

Numerical simulations, including Computational Fluid Dynamics (CFD), are used extensively in engineering for aerodynamics of aircraft and vehicles, hydrodynamics of ships, power plant modeling, turbomachinery, cooling of equipment, modeling blood flow through veins and arteries, and more [2]. Before these simulation results can be used, they must first be validated by comparison to experimental data or analytic solutions. With the exception of a few simple flows, analytic solutions are not available. The full-field velocity data provided by Particle Image Velocimetry (PIV) makes it an obvious choice for velocity validation measurements. PIV has the ability to provide instantaneous two- or three-component velocity fields which point measurement techniques, such as hot wire anemometry or Laser Doppler Velocimetry, can not. In numerical simulation validation, it is crucial to know the uncertainty for both the experimental and numerical data. A failure to do so can result in inaccurate models, flawed test results, and inefficient designs. In addition to CFD validation, PIV data are used to study flows by computing parameters such as drag and lift coefficients in addition to the velocity magnitude and direction. Like all experimental measurement techniques an understanding of the measurement uncertainty should be a high priority. The general practice of PIV is to ignore uncertainty, quote an unrelated study, or report a global uncertainty value which can be a gross overestimation is some regions and an underestimate in others.

The uncertainty of a PIV measurement is a very complex function of several parameters [1]. These parameters include, but are not limited to, particle image diameter, particle displacement, density, and velocity gradients. While there has been extensive study of the impact of these parameters on PIV uncertainty, it is exceedingly rare to see them employed in a PIV uncertainty analysis. The nature and impact of these parameters is such that the

uncertainty varies in space and time, so any attempt to determine the global uncertainty of data set post-priory is either impossible or is doomed to be very conservative.

Chapter 2

Literature Review

Before an attempt can be made to estimate the uncertainty of a PIV measurement a thorough understanding of both PIV algorithms and methods must be known. Once a base understanding of PIV algorithms are known, parameters can be identified which contribute to the uncertainty of the measurement technique.

2.1 Particle Image Velocimetry

PIV is a non-invasive optical measurement technique used to measure field velocities in a fluid flow. The velocity measurements are considered near instantaneous, as they average the velocity over very short period of time [3]. PIV measurements are limited to optically homogeneous fluids, meaning that the fluid has no significant interactions with the light, such as reflections. Optical homogeneity is also a requirement for transparency. Examples of optically homogeneous fluids include air and water. Small tracer particles, referred to as seeds, are added to the flow which are either the same density as the flow or are very small such that their motion is as close as possible to the actual flow motion. This gives the particles a drag force which is significantly higher than their gravitational force. Seeds are considered ideal when they exactly follow the fluid motion, do not alter the flow properties, and do not interact with each other. The tracer particles are required to have different optical properties than the fluids which they are added to so they reflect the light passing through the fluid. The position of these tracer particles are recorded at two instances in time and the flow velocity can then be inferred from their displacement [3]. The tracer particles are generally recorded using digital cameras and stored as intensity arrays. It is important to note that PIV does not track individual particles, but uses a numerical cross correlation to give an estimate of the most probable displacement of the particle image pattern (PIP).

Current PIV technology allows for the acquisition of particle image intensity arrays at rates up to 5000 or more times per second. From collections of these velocity measurements over time, average flow velocities and other parameters such as turbulent kinetic energy may be computed. General PIV techniques, methods and algorithms can be found in [1, 3–6].

2.2 PIV Algorithms

The PIV images are stored in pairs which have a specific time step between acquisition, dt. Transforming the recorded particle image pairs to a velocity vector field first involves dividing the images up into small sections called interrogation regions or windows. The cross correlation is calculated from each interrogation region in image 1 and its corresponding region in image 2 which gives the most likely displacement of the particles within that region. The PIV cross correlation can be computed directly from

$$C\left(r,s\right)=\sum_{i=1}^{M}\sum_{j=1}^{N}IA_1\left(i,j\right)IA_2\left(i+r,j+s\right) \tag{2.1}$$

where IA_1 and IA_2 are the intensity arrays for the interrogation regions of image 1 and 2 and M and N represent the interrogation region size (in pixels) [6].

Alternatively, a frequency domain method may be used to compute the cross correlation. According to the Wiener-Kinchin theorem, the cross correlation can be calculated as the product of the complex conjugates of the Fourier transforms of the interrogation regions [1]. To decrease computation time a Fast Fourier Transform (FFT) is used allowing us to replace Eqn. 2.1 with

$$C(r,s)=Re\left[FFT^{-1}\left\{FFT^{*}\left(IA_1\right)FFT\left(IA_2\right)\right\}\right] \tag{2.2}$$

where * denotes the complex conjugate and Re operator returns on the real part of the complex number. When using the FFT computation the interrogation regions IA_1 and IA_2 must be the same size, square, and have a length of 2^n where n is an integer [6]. Computation time is usually the deciding factor on which method is used to compute the

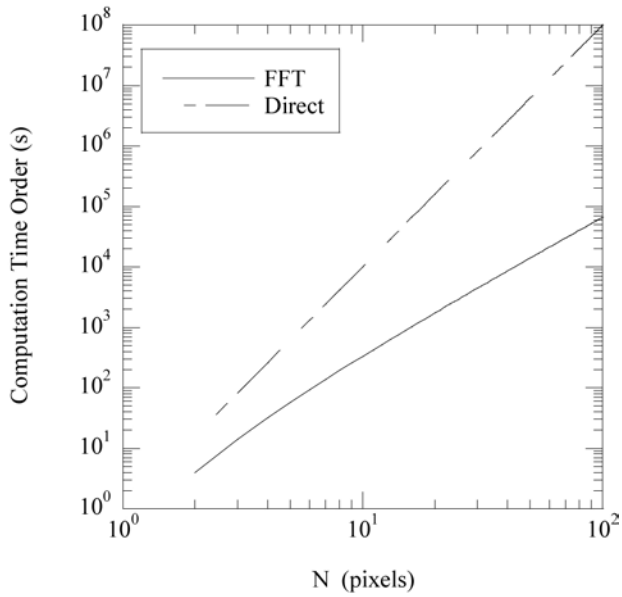

Fig. 2.1: Plot of the computational time order of magnitude against the interrogation window size (N). This plot assumes that the interrogation regions are square ($N \times N$).

cross correlation. If an interrogation window is used that is $N \times N$ pixels, the computation time needed by the FFT method goes as $O(N^2 log_2(N))$ while the direct computation goes as $O(N^4)$ [1,7,8]. The difference in computation time can be seen in Fig. 2.1.

The cross correlation $C(r, s)$ (see Fig. 2.2) outputs an array of values. The center of the region is used as a reference as it corresponds to zero displacement. The location of the maximum value of the $C(r, s)$ when referenced to the center gives the most likely pixel displacement of the region. The pixel displacement divided by dt gives the velocity estimation for that interrogation region. The particle velocity estimate from the cross correlation between two images is a low-pass filtered representation of the instantaneous particle velocities [9]; the velocity computed is the average velocity over dt, thus filtering out high velocity fluctuations which take place at time scales less than dt. This velocity will also lie between the average and median values of each particle velocity within the interrogation region. It should be noted that for the direct calculation of the cross correlation (Eqn. 2.1) the center of the region is located at $D_I/2$, but if the FFT method (Eqn. 2.2) is used, the center is located at $(D_I/2) + 1$. This subtle difference must be accounted for when a PIV algorithm is written.

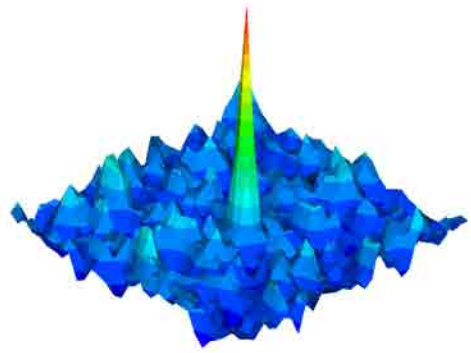

Fig. 2.2: A correlation map $C(r, s)$ example which can be calculated from either Eqn. 2.1 or Eqn. 2.2.

The cross correlation relies on the assumption that some of the particles from image 1 will remain in image 2. Theoretically the largest particle displacements that can result in a correlation computed from Eqn. 2.1 or Eqn. 2.2 is 1/2 of the interrogation region size. Practically it has been shown that a maximum particle displacement of 1/4 of the interrogation window will result in better correlations but limits the maximum displacement a particle can have [4].

Adaptive Local Window Shifting

Adaptive local window shifting is the processes of offsetting the interrogation windows by an integer displacement based on a priori knowledge of the local velocity. By offsetting the interrogation windows, the most likely displacement computed by the cross correlation will be less than one pixel. This method increases the probability that the interrogation window from image 2 will contain the same particles as the interrogation window from image 1, thus producing a stronger correlation.

To implement adaptive local window shifting, the velocity needs to be known before the computation may be preformed. This leads to multipass algorithms. The first pass is usually preformed with a large interrogation window (large enough to resolve the largest velocities) and no window shifting. This first pass gives an estimate of the velocity for each interrogation region in the flow. The second pass uses the estimated velocity from

the first pass as the integer displacements in the adaptive local window shifting method. An arbitrary number of passes may be used, each one providing a better estimate of the true particle displacement. Often in multipass algorithms, the interrogation window size is halved successively. By reducing the interrogation window size, it becomes possible to have large displacements but process with a small interrogation window on the final pass, decoupling dynamic range from spacial resolution [6, 10]. According to [6] the maximum particle displacement that should be used is still 1/4 of the size of the largest interrogation region, but should not exceed the final interrogation window size. Depending on the algorithm used and user inputs the spatial resolution of the vectors may change each pass. When a vector value is not available to offset the interrogation region of a pass interpolation methods are used to give a likely displacement at that location from neighboring values.

Subpixel Displacement Estimation

If the PIV algorithm stopped at the computation of the cross correlation described by Eqn. 2.1 or Eqn. 2.2, the displacement resolution would be limited to 1 pixel. To increase displacement resolution, subpixel displacement estimation methods are used. A common method fits a three point curve to the correlation peak along each axis, then the location of the curve maximum is computed. Gaussian (see Eqn. 2.3 and 2.4) and Parabolic (see Eqn. 2.5 and 2.6) curve fits use the maximum value of $C(r, s)$ and the points on either side to determine the peak maximum value to subpixel accuracy.

$$x_o = i + \frac{ln(C(i-1,j)) - ln(C(i+1,j))}{2ln(C(i-1,j)) - 4ln(C(i,j)) + 2ln(C(i+1,j))} \tag{2.3}$$

$$y_o = j + \frac{ln(C(i,j-1)) - ln(C(i,j+1))}{2ln(C(i,j-1)) - 4ln(C(i,j)) + 2ln(C(i,j+1))} \tag{2.4}$$

where the maximum value is located at $C(i, j)$.

$$x_o = i + \frac{C(i-1,j) - C(i+1,j)}{2C(i-1,j) - 4C(i,j) + 2C(i+1,j)} \tag{2.5}$$

$$y_o = j + \frac{C(i,j-1) - C(i,j+1)}{2C(i,j-1) - 4C(i,j) + 2C(i,j+1)} \tag{2.6}$$

Another prominent method is to use the maximum value of $C(r,s)$ and the surrounding values to compute a centroid of the peak (see Eqn. 2.7 and 2.8).

$$x_o = \frac{(i-1)C(i-1,j) + iC(i,j) + (i+1)C(i+1,j)}{C(i-1,j) + C(i,j) + C(i+1,j)} \tag{2.7}$$

$$y_o = \frac{(j-1)C(i,j-1) + iC(i,j) + (j+1)C(i,j+1)}{C(i,j-1) + C(i,j) + C(i,j+1)} \tag{2.8}$$

The relative location of the centroid is then used as the subpixel displacement [1]. The gaussian curve fit is generally used when the particle image diameters range between 2 and 4 pixels [6]. The centroid method has shown to be more accurate when the particle image diameters are greater than 4 pixels. None of the mentioned methods are very good at estimating subpixel displacements below particle image diameters of 2 pixels, and become completely useless when particle diameters are less than 1 pixel.

Window Deformation

Spurious vectors (vectors which do not represent to the true fluid velocity) will arise if the PIV algorithm is unable to match the PIP when computing the cross correlation. To compensate for loss of particle image pairs the second interrogation region is often deformed, allowing a stronger correlation to be computed in areas of high shear [11]. The direct cross correlation becomes

$$C(r,s) = \sum_{i=1}^{M} \sum_{j=1}^{N} IA_1(i,j)\, IA_2(i+r+\Delta x, j+s+\Delta y)\,. \tag{2.9}$$

The interrogation region's deformation, or window deformation, is usually based on a continuous image assumption. Because PIV images are stored digitally, interpolation schemes are needed to deform the region based on a continuous image. Interpolation schemes used to deform the interrogation region include linear, sinc, spline, third-order Lagrange, fourth-order Lagrange, and quadratic interpolation. The interpolation scheme is used to compute

Δx and Δy in Eqn. 2.9. The exact method to accomplish this varies depending on the interpolation scheme chosen. For example a linear interpolation will deform the interrogation region according to the truncated Taylor series

$$\Delta x = \Delta x(x, y) = \Delta x(x_0, y_0) + \frac{\partial \Delta x}{\partial x}(x - x_0) + \frac{\partial \Delta x}{\partial y}(y - y_0), \tag{2.10}$$

$$\Delta y = \Delta y(x, y) = \Delta y(x_0, y_0) + \frac{\partial \Delta y}{\partial x}(x - x_0) + \frac{\partial \Delta y}{\partial y}(y - y_0). \tag{2.11}$$

Window deformation begins with a standard cross correlation computation using a fairly large grid [11, 12] to predict a displacement field. From the predicted displacement field each interrogation region is deformed based on the interpolation scheme selected and a new velocity field is computed. This process can be repeated until the velocity field solution converges to an acceptable value. During each iteration the interrogation region size may be reduced to increase spatial resolution.

Windowing

To increase PIV accuracy, it is often useful to weight each interrogation region with a mask. The most popular weighting mask is the gaussian, although linear sloped mask are also used. The first step, if a gaussian mask is to be used, is to create a two-dimensional gaussian surface that is the same size as the interrogation window ($M \times N$)

$$\omega(i, j) = e^{-4\left(\frac{(i-M/2)^2}{(M/2)^2} + \frac{(j-N/2)^2}{(N/2)^2}\right)}. \tag{2.12}$$

The cross correlation calculation then becomes

$$C\,(r, s) = \sum_{i=1}^{M} \sum_{j=1}^{N} \omega(i, j) IA_1\,(i, j)\, IA_2\,(i + r, j + s) \tag{2.13}$$

replacing Eqn. 2.1 [13]. This will produce a $1 : 1$ gaussian mask. If weights are desired of different aspect ratios, one simply changes M and N to give the desired ratio, then adds zeros to the mask perimeter to make it the same size and shape as the interrogation

window (this is not the same as zero padding an interrogation region as it does not add high frequency noise if an FFT is used). If a non-unity aspect ratio is desired at a specific angle, a rotation matrix can be applied to the mask to rotate it to the desired angle.

2.3 Sources of Uncertainty in PIV

PIV uncertainty analysis is difficult because errors arise from both the experimental setup and the algorithm used to process data. Three forms of error are described by [14] and named as outlier, bias, and precision error. Bias error impacts every vector, while precision error impacts the mean velocity and statistics based on the mean. Outlier error may impact both bias and precision error.

2.3.1 Outlier Error

Outlier error is the result of a poor correlation [14] or when the highest magnitude peak in the correlation map does not correspond to the true displacement [6]. A good correlation (see Fig. 2.2) contains one large peak with low background noise while a bad correlation can take many forms but is generally defined by multiple peaks of the same order of magnitude and high background noise (see Fig. 2.3(a)) or may contain a single peak with a high magnitude ridge (see Fig. 2.3(b)). A poor correlation can be a result of many sources including improper particle density, strong velocity gradients, intensity value variations, and out of plane fluid motion [14, 15]. These sources all have one thing in common: they effect the PIV algorithm's ability to accurately match the PIP.

Outlier errors are generally larger then 1 pixel [14] which makes them easy to identify. Vectors affected by outlier error are called spurious vectors. Methods of identification for these spurious vectors include a global mean, local mean, local median, and the detectability (ratio of the highest magnitude peak to the second highest magnitude peak). The most efficient method of identification of these spurious vectors was found to be a local median filter [15]. If the spurious vectors are not removed they can easily dwarf other bias sources on an individual vector in time by offsetting its result from the true value. This large bias from the true velocity also affects precision error by mimicking a large velocity fluctuation

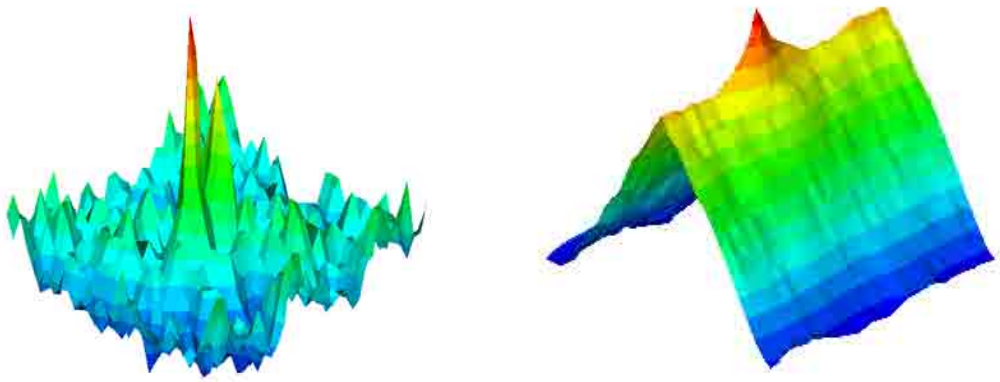

(a) (b)

Fig. 2.3: The cross correlation function $C(r, s)$ of: (a) a weak cross correlation with multiple peaks and high amplitude background noise and, (b) a weak cross correlation with a single peak and high magnitude ridge.

that doesn't exist.

The median filter first computes the spatial median and root mean square (RMS) velocity component values from the eight vectors surrounding the vector under consideration. The median is the middle value of the velocity values when they are arranged from smallest to largest magnitude. If the number of samples is even, then the median becomes the mean of the two middle values. The RMS is computed from

$$V_{RMS} = \sqrt{\frac{1}{N-1}\sum_{i=1}^{N}(V_i - V_{median})^2} \tag{2.14}$$

where N is the number of samples, V_{median} is the median velocity component, and V_i is one of the neighboring velocity components. The RMS is computed from the median velocity rather than the mean so if spurious vectors are contained within the data set they don't have a significant impact. The vector is identified as spurious if it does not satisfy for each velocity component

$$V_{median} - aV_{RMS} \leq V \leq V_{median} + aV_{RMS} \tag{2.15}$$

where V is the velocity component under consideration, and a is a user defined scale factor typically between 1 and 3.

The median filter can be used iteratively in a multiple pass scheme to remove a higher percentage of the spurious vectors. The first pass uses the local median filter as described above and identifies spurious vectors. Further passes then use the same local median filter as the first pass except all vectors that have been identified as spurious by previous passes are left out of the median and RMS calculations.

2.3.2 Bias Error

If a single measured value of velocity differs from the true velocity at that point and time then the difference is bias error. PIV velocity measurements are based on two parameters: computed particle displacement d_m and dt. The average velocity of the interrogation region over the time interval dt is then computed as

$$V = \frac{d_m}{dt}. \tag{2.16}$$

The dt value is orders of magnitude more accurately known then the displacement estimation from the cross correlation, therefore the uncertainty on the velocity measurement is assumed to be only a function of the displacement estimation [6]. Sources of uncertainty on the displacement include dynamic range issues, non-uniform interrogation regions, particle image diameter, particle seed density, shear, and more.

Dynamic Range and Spatial Resolution

Dynamic range is the maximum allowable displacement relative to the smallest displacements that can be measured. The minimum particle displacement that can be measured is a function of particle image diameter and the subpixel estimation method used. The maximum displacement that can be measured is limited by the interrogation window size because of the loss of correlation [1, 6] or "out-of-pattern" effect [14]. Loss of correlation reduces the number of particle image pairs contained within an interrogation region due to excessive in and out of plane motion, particles moving out of the interrogation region or out of the light sheet. The loss of particle image pairs in the interrogation region leads to

weak and false correlations. The maximum displacement is limited to 1/4 of the original interrogation region size [4] to minimize the loss of correlation. To increase dynamic range interrogation region size needs to be increased. This poses problems in flows where both high and low velocity values are expected, such as boundary layers. The time between image pairs must be short enough that the largest particle displacements do not exceed 1/4 of the interrogation region, without taking away our ability to resolve particles that move less than the minimum distance we can resolve. This resolution hinderance will create differing bias errors between high and low velocity regions of flow.

Spatial resolution can be thought of as the number of vectors contained within the vector field. The maximum theoretical spatial resolution possible that can be achieved is half the mean distance between particles [9] based on the Nyquist criterion. Higher spatial resolution can be achieved with smaller interrogation regions or, to an extent, the use of overlapping interrogation regions. Having high spatial resolution is especially important when velocity gradient information needs to be estimated.

Non-Uniform Interrogation Regions

Non-uniform flow conditions such as rotation and shear can be a large source of uncertainty in PIV measurements. PIV assumes that the interrogation windows have been resolved enough that the flow within the region is purely translational. Shear and rotation have the effect of making non-uniform flow within an interrogation window which violates the assumption of translational flow [1]. For these cases the cross correlation algorithm should give the spacial average particle velocity within the interrogation region. If shear or rotation is present within this region and the seed is not uniformly distributed, the predicted particle displacement will be biased toward areas of higher seed density. In regions of high shear, high velocity particles may leave the interrogation region, biasing the velocity result toward the lower velocity particles which remain in the region [1, 3, 16].

Large interrogation regions are less likely to produce spurious vectors due to a larger number of particles in the region but can preform very poorly when high shear is present in the region [17]. Smaller interrogation regions can more accurately resolve shear but contain

less information so are more prone to result in a spurious vector.

Reflections within the interrogation region from stationary objects, or streaks and sudden changes of the laser sheet intensity will correlate with itself. This usually results in a zero displacement measurement from the region [16].

Particle Image Diameter

The particle image diameter in PIV image pairs directly affects the algorithm's ability to estimate subpixel displacements. Optimum particle image diameters have been given by many authors which ranging from 2 pixels [1] to over 6 pixels [16]. The reason that more than one optimum particle image diameter are reported is that it is dependent on the sub pixel estimation method used. The 2 pixel optimum reported by [1] is based on a three point gaussian estimate method while the 6 pixel optimum from [16] uses a thin shell smoothed spline technique and claims that other researches haven't accounted for high shear within an interrogation region. Other subpixel estimation methods such as centroid techniques require larger particles (> 4 pixels) for increased accuracy [6].

It is recommended by [16] to have a distribution of particle image diameters in the image pair. The distribution of particle image diameters increases the probability of a unique PIP within the interrogation region. Larger particles have been shown to reduce error when high levels of shear are present within a flow. As particle image diameters decrease in size the ability to predict subpixel displacements diminish. Particle images that are too small (≤ 1 pixel) result in an effect known as peak locking. Peak locking is characterized by particle displacements being biased toward integer pixel values [1] producing sometimes periodic displacement counts when a histogram is made of interrogation region displacements [16]. Peak locking also contributes to precision error and its effects are discussed later.

Particle Density

The ability of a PIV algorithm to correctly match the PIP for an interrogation region of an image pair is dependent on the information available. As more particle images are contained within an image pair this information increases, resulting in a higher probability

of a valid velocity vector [1]. The number of particle image pairs contained within an interrogation region is dependent on the number of particles, in plane motion, and out of plane motion. The number of particles in the flow is controlled via the experimental set up while in plane and out of plane motion is controlled by the dt as discussed in the dynamic range section. The number of particles divided by pixel area is known as particle density.

According to [1] a minimum of 3 to 4 particle images should be contained within an interrogation region. For flows with strong regions of shear, [16] recommends a high seed density and found that in flows with low shear the seed density was not critical. Because PIV algorithms match patterns rather than track particles, the background of an image is just as important as the particle images [16], thus high seed densities which result in overlapping particle images can hinder the algorithms ability to match the PIP uniquely. If the seed density within the flow is too high the seed may also affect the flow characteristics of the fluid being studied or begin to interact with each other [3, 6].

Other Sources of Bias

According to [3, 13], the maximum correlation value (most likely displacement) always deviates from the true value toward smaller displacements. This effect is proportional to the width of the correlation peak and particle image diameter. A typical bias for a 32×32 interrogation window suffering from this is about 0.1 pixels [3]. This bias is caused by the cross correlation method. For detailed analysis of this error see [13].

A source of error that doesn't fit into the specific types of error previously listed involves the type of PIV algorithm used. When computing the cross correlation two dominate methods are used, a direct calculation and a method utilizing a FFT. The FFT method assumes that the intensity profile within the interrogation region is periodic making it susceptible to aliasing problems, a phenomena which makes high frequencies show up as low frequencies. Since the FFT method limits the size and shape of the interrogation regions they are often padded with zeros to change the shape and size. Zero padding can create high frequency noise in the interrogation region due to sharp discontinuities between the pixel intensity values and the added zeros [1]. Using the direct calculation allows repositioning

of the second interrogation region for each displacement [7] as well as increasing the size of the second interrogation region to reduce loss of correlation [14]. The error associated with these differences can manifest as outliers or mean bias errors and effect precision uncertainty. Errors stemming from the PIV algorithm will be considered as a bias error for this analysis as it effects each individual vector.

2.3.3 Precision Error

It is important to note that precision error is an error on the mean velocity, not an individual measurement. Sources of precision error include: camera "dark current" noise, non-linear and non-uniform camera response, non-uniform illumination, non-uniform reflection, camera cable noise, and digitization error [14]. These sources all produce noise in the PIV images. Noise in a PIV image produces error in pixel intensities, which lead to errors in particle locations. Other sources include peak locking, and velocity fluctuations present in the flow [18]. These sources of precision error indicate that the mean velocity is not being sampled accurately.

Precision error is not necessarily bad and may be used to determine if a fluid flow is laminar or turbulent. The previously stated sources of precision error can be summed up into two main sources, noise and velocity fluctuations. For turbulent flows the velocity fluctuations will generally be significantly higher in magnitude than the noise, thus dominating the precision uncertainty [18]. For laminar steady flows however image noise becomes the substantial component of precision error. Examples of velocity fluctuations and noise can be seen in Fig. 2.4.

Precision uncertainty has been observed to appear spatially correlated, which is due to interrogation regions sampling the same flow structures as neighboring regions, non-random samples [18]. This can be especially evident in turbulent flows, of which the precision error is often far greater than the bias.

Peak locking can make precision error appear to be smaller than it actually is. This is because all displacements are biased toward integer pixel values, creating a high number of similar displacements in steady regions of flow [9]. If particle displacements are too large,

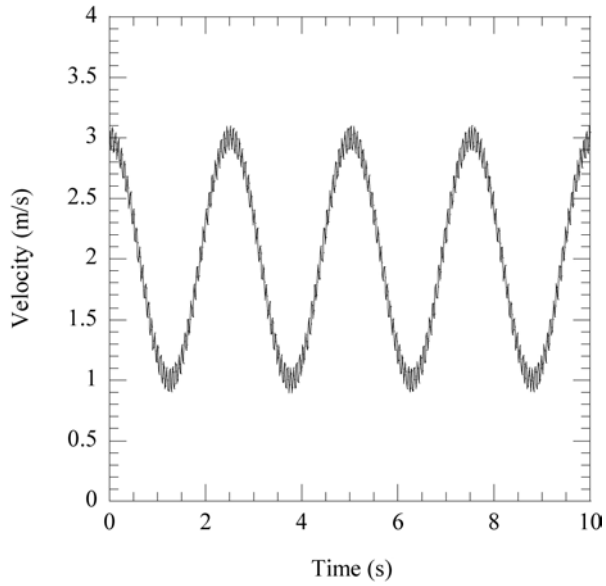

(a)

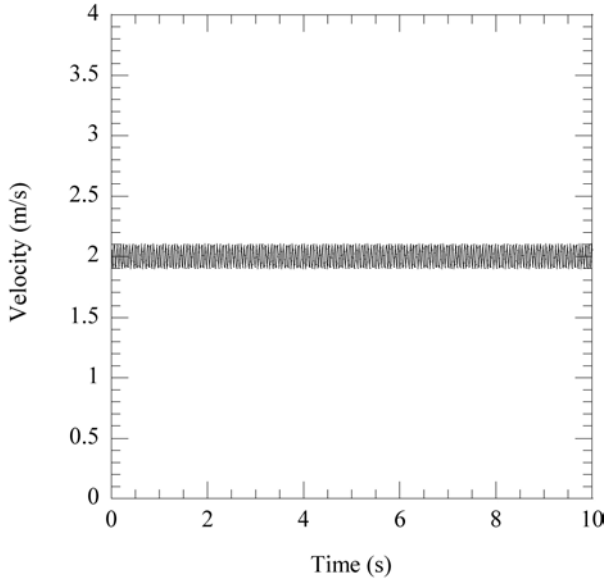

(b)

Fig. 2.4: PIV velocity over time (a) for low frequency sinusoidal turbulent velocity fluctuations data with high frequency sinusoidal noise and, (b) constant laminar velocity data with high frequency sinusoidal noise.

then the precision uncertainty returned can also misrepresent the true error. This is due to the low-pass filter nature of the cross correlation. High frequency velocity fluctuations at time scales less than dt are averaged out.

Chapter 3

Objectives

The objectives of this thesis are as follows:

1. Identify and select contributors to PIV error. Based on [1], the following contributors have been selected:
    - Particle image size
    - Particle seeding density
    - Shear rate
    - Displacement
2. Generate synthetic images for flows that contain various particle image sizes, seeding densities, shear rates and displacements.
3. Compute vector fields from the synthetic images and compare them to the known solutions to find the errors as a function of each of the parameters.
4. Compute uncertainty estimates from the distribution of errors (step 3) and formed into the Uncertainty Surface.
5. Estimate particle displacements, size, and density as well as flow shear.
6. Combine the estimates (step 5) with the uncertainty surface (step 4) to determine the uncertainty for each vector.
7. Verify the method's effectiveness by comparing the true solution of known flows to the calculated velocities and their uncertainty band widths.

Chapter 4

Procedures

An effort to develop a framework to estimate the uncertainty of every PIV vector based on the measured flow as well as the raw image data is given. I begin by estimating the uncertainty of a publicly-available PIV code (PRANA, developed at Virginia Tech, [19–21]), using the Standard Cross Correlation (SCC) and Robust Phase Correlation (RPC) algorithms as a function of several well-accepted error sources. The method (which is integrated into the PIV code) measures the parameters that are known to influence uncertainty. Once these parameters have been quantified, an estimate of the velocity uncertainty is made for each velocity vector in space and time. The influence of these parameters on uncertainty is determined from error analysis generated using synthetic images of known flow fields.

4.1 PIV Algorithms

It is important to make the distinction between PIV software and a PIV algorithm. The PIV algorithm consists of a specific series of operations which are carried out on arrays of discretized pixel intensities. These pixel arrays are a representation of an area of fluid flow which contain seed particles that are illuminated by a light source. Examples of these operations include Fourier-based cross correlation, gaussian subpixel displacement estimators, windowing, multipass, etc. The logistics of data storage, manipulation, and implementation of the specific operations in specified order describe PIV software. If two instances of PIV software use the same algorithm, they must produce identical results. An understanding of the distinction between PIV algorithms and software is vital when considering the application of the results from any PIV study. When duplicating a published PIV result with a different algorithm, one will not be able to identically match the results. Also note that PIV processing with nearly any software requires the user to make dozens

of choices on the algorithm features as well as the order in which they are executed. As a result, even with the same software, it is unlikely that two users will use identical algorithms.

4.2 Uncertainty Estimates for Specific PIV Algorithms

It is first important to make a distinction between error and uncertainty, since, while there have been many studies of PIV error (or accuracy), there have been few on PIV uncertainty. According to [22], "An error δ is a quantity that has a particular sign and magnitude, and a specific error δ_i is the difference caused by error source i between a quantity ... and its true value....Uncertainty U is thus an estimate: a $\pm U$ interval is an estimate of a range within which we believe the actual (but unknown) value of an error δ lies."

This study attempts to quantify the uncertainty of PIV-computed velocity vectors automatically. It is not the intent of this study to prove the superiority of one PIV algorithm over another. The original intent of this study was to produce a universal uncertainty model which could be distributed with any PIV software. By looking at the PIV Challenge results [23–25] it is clear that this cannot be accomplished. These studies show that various PIV algorithms have different errors for identical input. It is also apparent that different algorithms are more sensitive to certain image parameters than others, such as shear, particle diameter, and density. Because of this, a single PIV uncertainty model for all algorithms cannot provide realistic results.

To further demonstrate the need for individualized uncertainty values for each PIV algorithm, synthetic images are processed using LaVision's DaVis 7.2.2 and PRANA, which was developed at Virginia Tech [19–21]. The average error of velocity vectors from a uniform flow based on subpixel displacement only was computed for flows processed by the two PIV algorithms and are shown in Fig. 4.1. The images processed with DaVis used three passes with the first pass interrogation regions 64 pixels square and the final pass 16 pixels square. A circular window was applied to each pass. The images are processed with PRANA using a Multigrid Standard Cross Correlation routine with gaussian windowing and three passes similar to the one ones used by DaVis. Not only do the velocity error values differ, but the

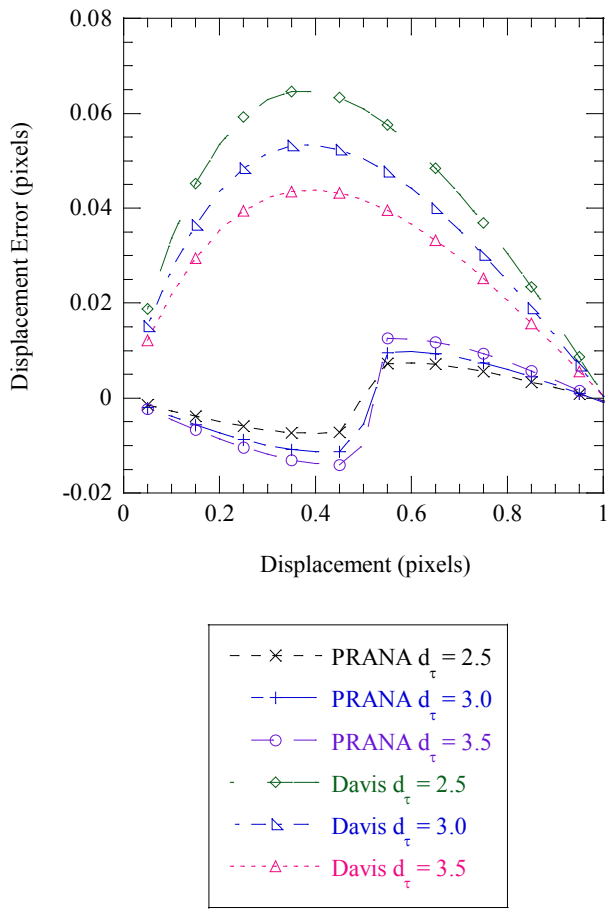

Fig. 4.1: Average subpixel displacement error as computed by DaVis 7.2.2 and PRANA for different diameters, d_τ, at a particle image density of 0.0293 particles/pixel^2.

shape and sign of the error curves are significantly different between the different algorithms.

4.3 Uncertainty Estimation

Using a 1-D equation for clarity, the calculation of velocity in PIV measurements comes from the approximation

$$u = \frac{dx}{dt} \approx \frac{\Delta x}{\Delta t}. \tag{4.1}$$

The uncertainty of u can come from both the displacement Δx and the time increment Δt. Using the Taylor Series Method for uncertainty propagation [22], the combined uncertainty

estimate for the velocity, assuming that the uncertainty of Δx and Δt are not correlated, is

$$u_u = \sqrt{\left(\frac{\partial u}{\partial \Delta x} b_{\Delta x}\right)^2 + \left(\frac{\partial u}{\partial \Delta t} b_{\Delta t}\right)^2} \tag{4.2}$$

where $b_{\Delta x}$ and $b_{\Delta t}$ are the uncertainty estimates of Δx and Δt. The uncertainty of Δt is small enough that it is assumed negligible, so the uncertainty of u becomes proportional to the displacement uncertainty $b_{\Delta x}$. Eqn. 4.2 simplifies to

$$u_u = \left(\frac{1}{\Delta t}\right) b_{\Delta x}. \tag{4.3}$$

The Monte Carlo Method (MCM) for determining the combined uncertainty assumes a Probability Density Function (PDF) for each input variable. The values of these variables are randomly chosen according to the assumed distribution, and the solution is computed from the data reduction equation. The calculation is repeated until the standard deviation is converged [22], which is the uncertainty estimate that includes all correlation effects.

The data reduction equation for PIV is given by its algorithm. The inputs to the data reduction equation are arrays of pixel intensities, and the output is a vector. Pixel intensities in a single image are correlated with each other through particle image diameter and density. The pixel intensities between image pairs are correlated with each other through particle displacement, shear, and rotation. For most PIV algorithms, it is not beneficial to develop an analytic expression of the data reduction equation. If an interrogation region were only 8 pixels square, the data reduction equation becomes a function of $2(8)^2 = 128$ pixel intensity values. Because the data reduction equation is a function of many variables, all of which are correlated, a MCM to determine a combined uncertainty estimate is selected. The random variable in the MCM simulation is particle location, which is selected from a uniform distribution.

4.3.1 Synthetic Images

"Synthetic images" are computer generated PIV image pairs, sometime called Monte

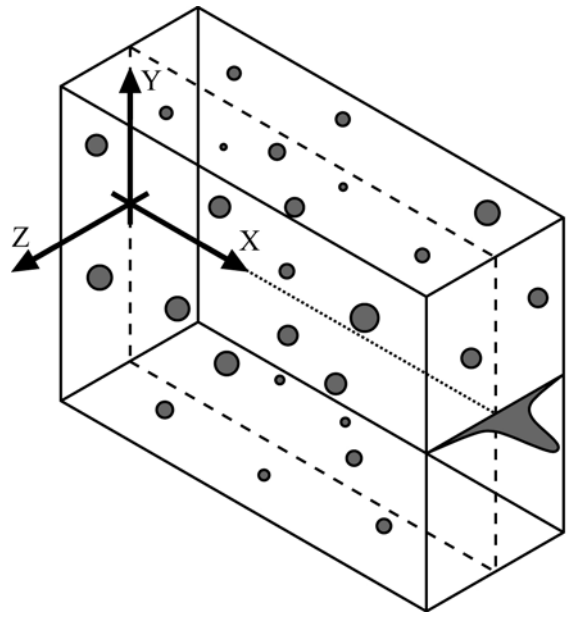

Fig. 4.2: Volume showing particles and gaussian laser sheet profile [1].

Carlo simulations [1,4,6]. Using synthetic images based on known flow data (from analytical solutions or numerically computed flow fields) makes it possible to know the exact solution, and true error, for specific cases. Synthetic images also allow for control of the particle displacement, image background noise, particle size, particle density, and particle intensity.

In creating synthetic images, a random number generator (based in a uniform distribution) is used to populate a volume with particles (see Fig. 4.2), the random numbers giving the particle locations. A simulated laser sheet passes through the center of the volume which has a gaussian intensity profile. The purpose of the laser sheet in the simulation is the give the particles a peak intensity. Once the volume is populated with enough particles to reach the desired particle density a second volume is created in which all particles are displaced according to the desired velocity field. It is important that the volume being populated is larger than the desired image. This allows for particles to move in and out of the image pair as shown in Fig. 4.3. Each volume is then digitized (particles are changed into pixel intensities).

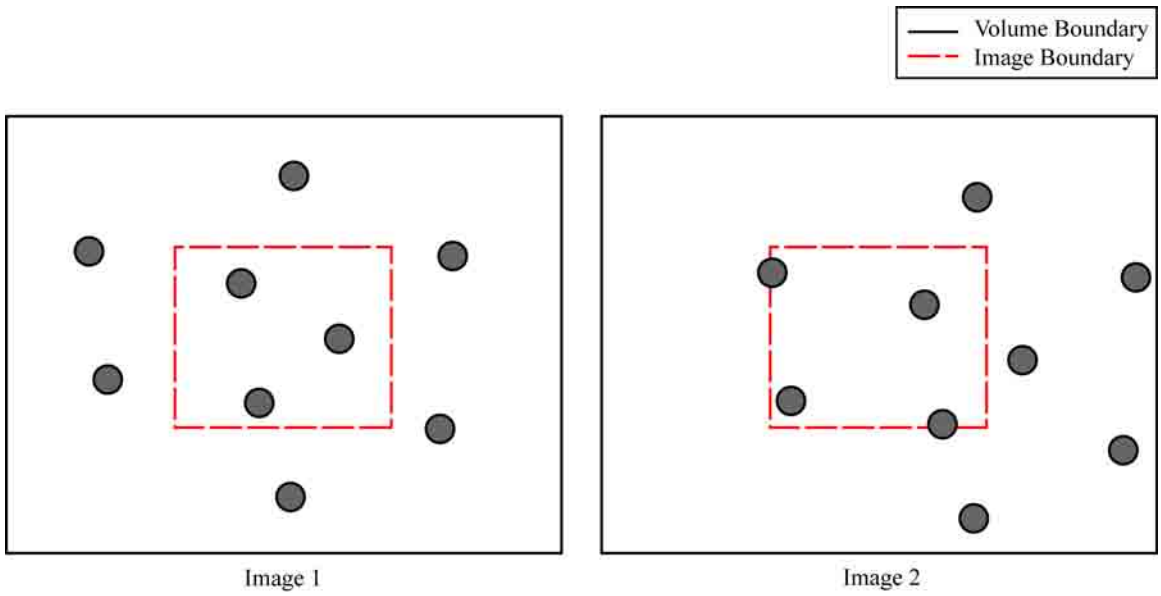

Fig. 4.3: Two images of the same space as shown as particles move through a volume. It is illustrated that the volume containing particles needs to be larger than the images desired.

The digitization process starts with the apparent particle diameter as seen by the camera. This is found from

$$d_\tau = \left(M^2 d_p^2 + d_s^2\right)^{1/2} \tag{4.4}$$

$$d_s = 2.44\,(1 + M)\,f^{\#}\lambda \tag{4.5}$$

where $f^{\#}$ is the lens aperture number, λ is the laser wave length, M is the magnification, and d_p is the actual particle diameter [6]. Then the particle intensity can be computed based on the gaussian laser sheet

$$I_{pp}(z) = I_{lp} e^{-8z^2/d_l^2} \tag{4.6}$$

where I_{lp} is the peak intensity and d_l is the sheet thickness. As a result of using a gaussian laser sheet with finite thickness, particles moving in the z-direction (see Fig. 4.2) change peak intensity. Once the peak particle intensity has been calculated the particle intensity profile can be computed. The particles are assumed to produce a gaussian light profile

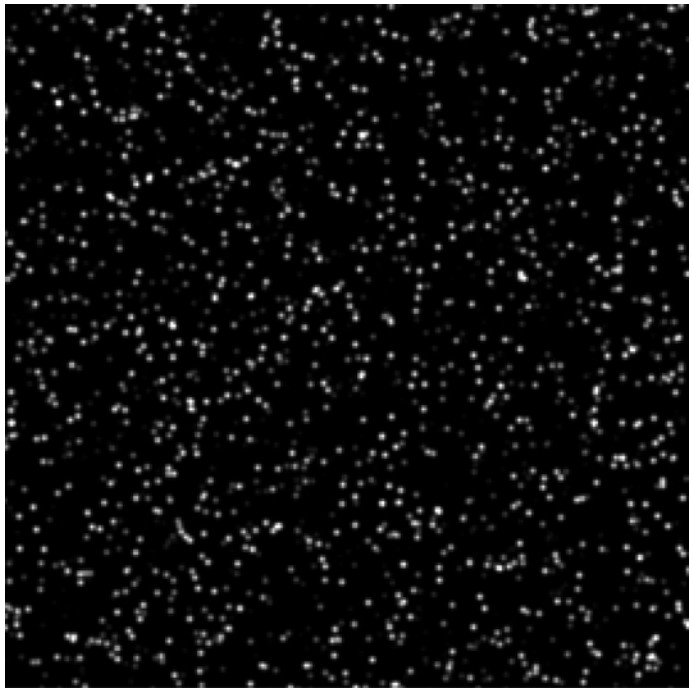

Fig. 4.4: A syntectic image that is 256×256 pixels with 3 pixel diameter gaussian particles, and a 1mm thick light sheet.

according to

$$I_p(x, y) = I_{pp} e^{-8\left[(x-x_0)^2+(y-y_0)^2\right]/d_\tau^2} \tag{4.7}$$

where x_0 and y_0 are coordinates of the particle center. Eqn. 4.7 can be used to define the intensity contribution of a particle to the entire image, however for this work, any values of $I_p < 1 \times 10^{-8}$ will be neglected. This simplification saves considerable computational time to generate the synthetic images. Now that the particle intensity profile is defined (Eqn. 4.7), it can be integrated over the area of a pixel to determine that specific pixel's intensity

$$I = \int_{y_1}^{y_2} \int_{x_1}^{x_2} I_p(x, y) dx dy. \tag{4.8}$$

The images then become the sum of all the particle intensity profiles. A finished image frame without background noise can be seen in Fig. 4.4. Background noise can be included

to the images by adding to the image

$$I_N(i,j) = I_{mean} + I_{fluct} rand(-1,1) \tag{4.9}$$

where I_{mean} is a constant background noise level, I_{fluct} is a fluctuation noise amplitude that multiplies $rand(-1,1)$ which returns a random number between -1 and 1 [6].

Five flows are studied ranging from simple to complex: uniform flow, constant gradient, Couette-Poiseuille flow between plates, Burger's Vortex flow, and Direct Numerical Solution (DNS) for a laminar separation bubble from the 2005 PIV challenge [25].

A uniform velocity flow can be created by displacing all particles by the same specified magnitude for each velocity component. Mathematically it can be expressed as

$$\mathbf{v} = \begin{bmatrix} u \\ v \\ 0 \end{bmatrix}. \tag{4.10}$$

The uniform velocity flow field allows for study of PIV errors without gradients, rotation, and no out of plane loss.

The linear velocity profile (constant gradient) is defined as

$$\mathbf{v} = \begin{bmatrix} u + y\left(\frac{du}{dy}\right) \\ 0 \\ 0 \end{bmatrix}. \tag{4.11}$$

The linear velocity profile allows the study of velocity calculations in the presence of constant shear without rotation and out of plane loss.

The combined Couette-Poiseuille flow is a laminar one-dimensional flow driven by a constant pressure gradient and moving upper wall with no slip boundary conditions at each

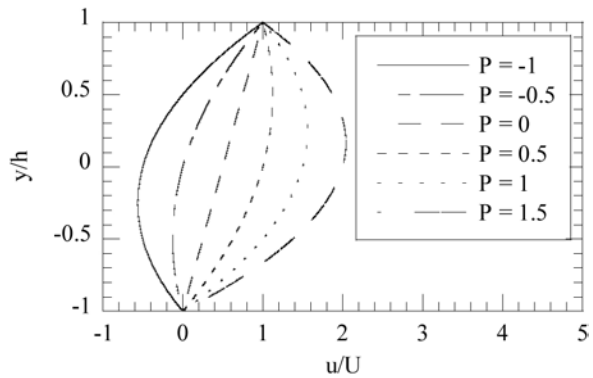

Fig. 4.5: Combined Couette-Poiseuille flow velocity profiles for varying pressure gradients.

wall. The flow field can be expressed as

$$\frac{u}{U} = \frac{1}{2}\left(1 + \frac{y}{h}\right) + P\left(1 - \frac{y^2}{h^2}\right), \qquad P = \left(-\frac{dp}{dx}\right)\frac{h^2}{2\mu U} \tag{4.12}$$

where U is the velocity of the upper wall, and h is the half distance between plates [26]. The velocity vector then becomes

$$\mathbf{v} = \begin{bmatrix} u \\ 0 \\ 0 \end{bmatrix}. \tag{4.13}$$

The Couette-Poiseuille flow maintains a constant profile in the x and z direction. Velocity profiles for the combined Couette-Poiseuille flow can be seen in Fig. 4.5. By generating synthetic images from this flow field, the effects of non-constant shear can be examined without out-of-plane motion of the PIV algorithm.

A Burger's Vortex is a vortex model which assumes the fluid is steady, axis-symmetric, with small axial gradients of physical quantities. The flow velocity is described by

$$\frac{V_\theta}{V_{\theta b}} = \frac{R_{eb}}{2\left(1 - e^{-R_{eb}/2}\right)}\frac{r}{b}, \qquad R_{eb} = -\frac{bV_{rb}}{\nu_t} \tag{4.14}$$

$$\frac{V_r}{V_{rb}} = \frac{r}{b} \tag{4.15}$$

where b is the radius of the vortex, and V_{rb} and $V_{\theta b}$ are cylindrical components of velocity at $r = b$ [27]. Converting to cartesian coordinates

$$\mathbf{v} = \begin{bmatrix} V_r cos(\theta) - V_\theta sin(\theta) \\ V_r sin(\theta) + V_\theta cos(\theta) \\ 0 \end{bmatrix}. \tag{4.16}$$

Producing synthetic images that follow this flow field allow for the study of the effects of a rotational flow field without out-of-plane motion on the PIV algorithm.

The final flow field produced is that of a DNS for a laminar separation bubble from the 2005 PIV challenge case B [25]. Rather than computing the flow velocity at each particle location, a table look up was used based on the DNS results for the flow.

Background noise was added to each image at three different levels. The first level is zero noise, which is intended to give a best case scenario. The second noise level is meant to approximate the actual noise level in the PCO sensicam QE 12 bit CCD camera. To approximate the noise produced when recording images with this camera 100 image pairs are taken of air with no seed particles illuminated by a New Wave Research Solo PIV III ND-Yag Laser dual cavity laser. A histogram of the pixel intensities is generated to show the noise distribution. The histogram x-axis is normalized by the maximum pixel intensity (4095), and the y-axis is normalized by the total number of pixels recorded. The normalized histogram is fitted with a normal distribution,

$$y(x) = Ae^{-\frac{(x-\mu)^2}{2\sigma^2}}, \tag{4.17}$$

with average $\mu = 1.011e^{-2}$ and standard deviation $\sigma = 5.96e - 4$. Random samples are then taken from this normal distribution and added to each image to simulate the background noise of the PCO sensicam camera. The third noise level is meant to approximate the actual noise of the Photron FastCam APX RS 10 bit CMOS camera. Following the same procedure that was used for the second noise level, 100 image pairs are taken of air with no seed illuminated by a Photonics ND-YLF single cavity laser. A histogram is made and

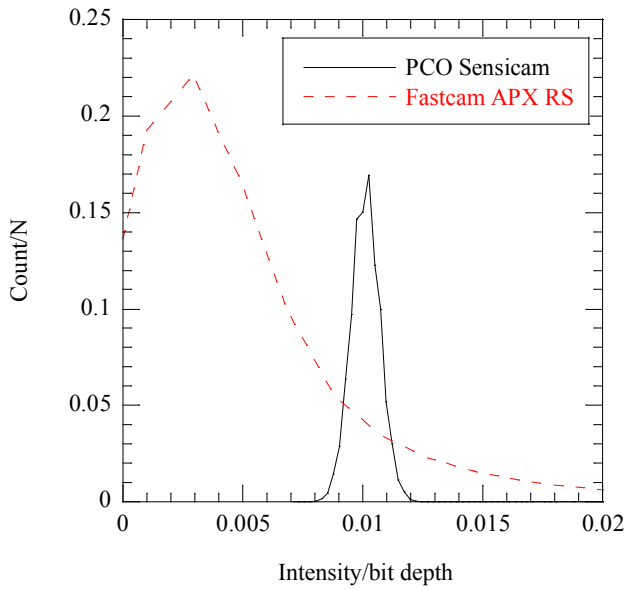

Fig. 4.6: Normalized histogram of background noise from PCO sensicam QE CCD and Photron FastCam APX RS CMOS cameras.

normalized in the same manner as the second noise case and fitted with a normal distribution of mean $\mu = 2.834e^{-3}$ and standard deviation $\sigma = 3.55e^{-3}$. This normal distribution is then randomly sampled to produce background noise for the third case. The normalized histograms from these cameras are seen in Fig. 4.6.

4.3.2 Generating the Uncertainty Surface

According to [1], the main sources of error in PIV are particle image density, in-plane loss, out-of-plane loss, particle diameter, particle displacement, and shear. In-plane loss and out-of-plane loss will be considered as criteria to exclude data and are not considered in this thesis. The others sources of error will be the focus of the current study to estimate uncertainty values. A multipass PIV algorithm is used so only the subpixel displacement will be considered as contributing to the uncertainty value. This assumption was tested and found true 97% of the time. The effects of background noise are not included in the uncertainty surface because they are considered negligible compared to noise created by the FFT correlation [1]. The uncertainty data given by [1] is not used since it is specific to the

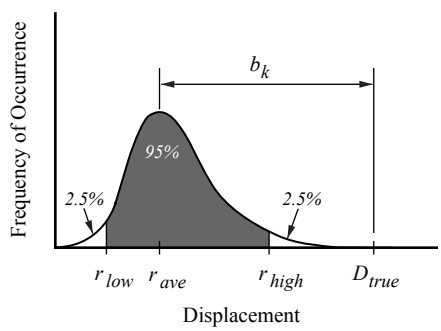

Fig. 4.7: Theoretical histogram showing the distribution of computed displacements and the true displacement D_{true}. r_{ave} is the average displacement that is calculated by the PIV algorithm. The value b_k is the systematic uncertainty value. r_{low} and r_{high} are the upper and lower bounds in which 95% of the data are contained.

algorithm that was used to generate it.

For interrogation regions experiencing identical true displacements (made from synthetic images) the same vector is not always computed from interrogation region to interrogation region. Even though the data reduction equation is the same for each region, the inputs of pixel intensities differ. The pixel intensity arrays vary because particles are randomly distributed throughout the flow. Another difference arises because the Fourier-Based Cross-Correlation computation introduces noise into the correlation map [1], which is dependent on the input pixel intensity arrays. The distribution of these displacements is used to compute a 95% confidence interval (see Fig. 4.7).

There exist unique upper, r_{high}, and lower, r_{low}, values of the precision uncertainty (since the distribution of PIV error is, in general, not symmetric) for each data point and a systematic uncertainty value b_k. The systematic uncertainty is computed as the difference between the true displacement D_{true} and the average computed displacement r_{ave}. The

precision uncertainty values are calculated by computing the area under the probability curve, since the curve is a histogram, integration is accomplished by summing the number of samples. The lower limit r_{low} is the difference between r_{ave} and the point at which the area under the curve is 2.5% of total area under the histogram. Similarly, the upper bound r_{high} is the difference between the point in which the area under the curve is 97.5% of the total area and r_{ave} [22].

The combined uncertainty estimate for the lower uncertainty bar limit can be computed as Eqn. 4.18 and the upper bound as Eqn. 4.19.

$$U_r^- = \sqrt{r_{\text{low}}^2 + b_k^2} \tag{4.18}$$

$$U_r^+ = \sqrt{r_{\text{high}}^2 + b_k^2} \tag{4.19}$$

It should be noted that no assumptions have been made about the shape (PDF) or location of the displacement distributions. Although the b_k is considered a symmetric uncertainty value, it is represented as having a unique upper and lower bound with magnitudes that are identical.

It is often desired to compute time statistics for PIV velocity measurements. An estimate of the uncertainty on the mean of a velocity vector can be computed as

$$\bar{U}_r^- = \sqrt{\left(1.96\frac{s_x}{\sqrt{N}}\right)^2 + \frac{1}{N}\sum_{i=1}^{N}\left(U_{r_i}^-\right)^2} \tag{4.20}$$

$$\bar{U}_r^+ = \sqrt{\left(1.96\frac{s_x}{\sqrt{N}}\right)^2 + \frac{1}{N}\sum_{i=1}^{N}\left(U_{r_i}^+\right)^2} \tag{4.21}$$

where s_x is the standard deviation of the velocity at a point in space and $U_{r_i}^-$ and $U_{r_i}^+$ are the uncertainty values for each velocity measurement used to compute s_x.

The data are recorded for multiple particle image diameters, densities, displacements, and velocity gradients creating an input parameter space which is defined in Table 4.1.

The number of data points to be used was determined after a convergence study was

Table 4.1: Range of the Computed Uncertainty Estimates

Input Parameter	Lower Limit	Upper Limit	Step size
Particle Image Diameter (pixels)	0.5	5.0	0.5
Particle Image Density (particles/pixels^2)	0.0098	0.0391	0.0098
Particle Image Displacement (pixels)	-1.0	1.0	0.1
Gradient (pixels/pixel)	0.00	0.20	0.02

Table 4.2: PIV Processing Parameters Used to Compute the Uncertainty Surface

Pass	Grid Resolution x,y (pixels)	Grid Buffer x,y (pixels)	Window Resolution x,y (pixels)	Window Size x,y (pixels)	Validation
1	8,8	8,8	64,64	128,128	none
2	8,8	8,8	32,32	64,64	none
3	8,8	8,8	16,16	32,32	7,7;7,7

performed. The results are shown in Fig. 4.8. The images are all proceed using the same inputs (the same PIV algorithm). Three passes are used in a Multipass (DWO) routine. The parameters of each pass are summarized in Table 4.2. The median filter version of the universal outlier detection method [28] was used as the validation method to post process the data. No filtering was performed based on the correlation peak magnitude. Note that validation was only preformed on the final pass, however this is not technically correct. The DWO routine uses validation steps between each pass, they are not listed as the user is not required to specify them. Vectors that are identified as outliers are removed. The interrogation regions were spaced far enough apart that even with window shifting there was no interrogation region overlap. Thus, the particles in each image pair are only sampled once creating independent vectors. It was surmised that $10,000$ vectors for each point in the uncertainty surface were sufficient for statistical convergence.

Using the statistics of the 10,000 samples along with Eqn. 4.18-4.19, a 4-D uncertainty surface was generated. Some of the results are presented by holding two variables constant and varying the other two. Figure 4.9 shows U_r^+ for no gradient and 0.8 pixel displacement. Figure 4.9 illustrates that the uncertainty estimate is almost constant with diameter and density with the exception of small particle image diameters and low particle density.

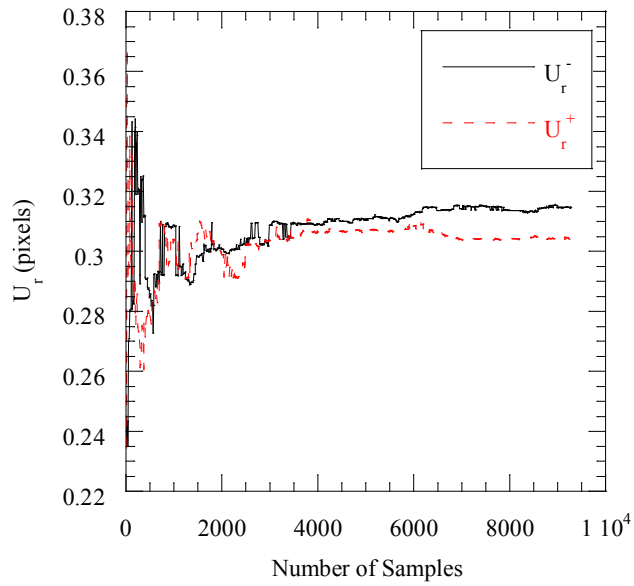

Fig. 4.8: Values of U_r^- and U_r^+ for different numbers of samples used to compute them.

Figure 4.10 shows U_r^+ for 2.50 pixel particle image diameter and 0.0195 particle/pixel^2 density and shows that the uncertainty estimate is a weak function of displacement (with maximum uncertainties near ± 0.05 pixels) but is sensitive to shear.

4.3.3 Computational Cost

At this point the resource cost should be mentioned, although computational performance is not a concern at this time. The computational time to generate the uncertainty surface is large; nearly 100,000,000 vectors were computed to generate the surface. The synthetic images are generated from a parallel FORTRAN code which utilized MPI, and an image file writing library. The images were made such that they are large enough that $10,000$ vectors can be computed from each image pair. The interrogation regions are spaced far enough apart that even with window shifting there is no interrogation region overlap, the particles in each image pair are only sampled once creating independent vectors. The images were generated on a 24 client cluster which took approximately 7 days. The processing of the images using PRANA, which is written in MATLAB, took approximately 4 days

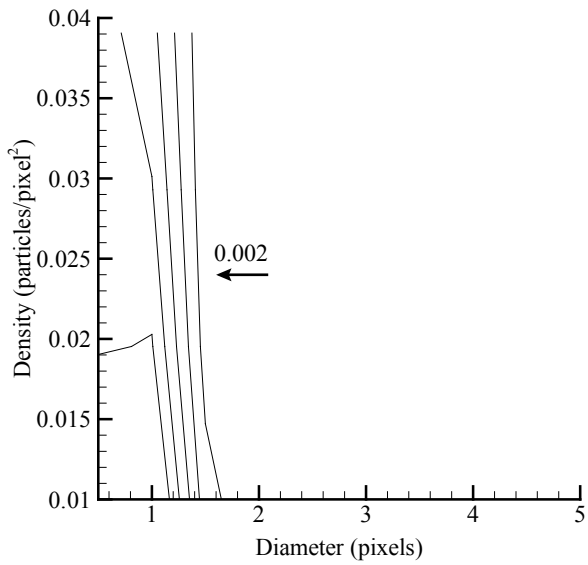

Fig. 4.9: U_r^+ contours as a function of particle image diameter and seeding density for no gradient and 0.8 pixel uniform displacement for the SCC method. The contour increment is 0.002 pixels.

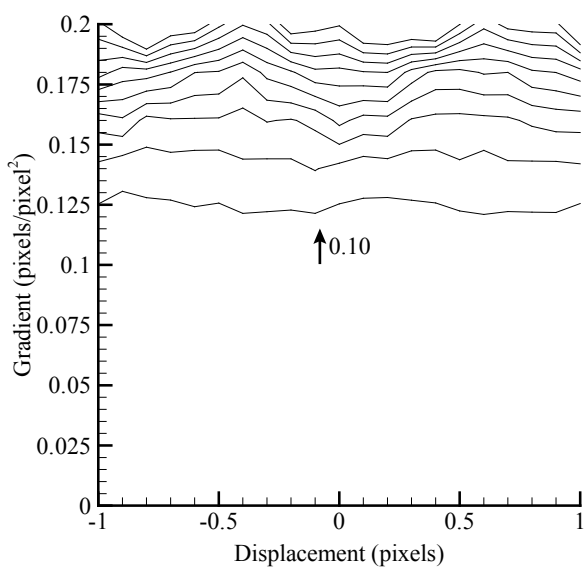

Fig. 4.10: U_r^+ contours as a function of displacement and gradient for 2.50 pixel particle image diameter and 0.0195 particle/pixel^2 density. The contour increment is 0.10 pixels.

to complete using 40 clients. For each PIV algorithm, the uncertainty surface only needs to be computed once, unless changes to the algorithm are made. Once implemented within the PIV software the uncertainty estimate for each interrogation region takes an amount of time on the same order as the PIV correlation step computation.

4.4 Uncertainty Comparison

Several earlier studies have examined the error of PIV as a function of various parameters. Some of these results [1] will now be compared to our uncertainty surface to demonstrate that the present uncertainty surfaces are unique, but have similar magnitudes to previously published studies. The RMS error reported by [1] is never defined, but using a common definition, it is essentially a $1-\sigma$ uncertainty. Therefore, to make a comparison to the current results, ϵ_{rms} should be multiplied by 1.96 to obtain a 95% uncertainty. In most cases, Raffel did not report the bias uncertainty and only very limited data are available for direct comparison. Since both PRANA algorithms had similar behavior, only the SCC results are compared.

The accuracy of PIV has been widely reported as being maximized for a particle image diameter near 2 pixels, as shown in Fig. 4.11. The PRANA algorithm is somewhat more accurate for this case than Raffel's code and did not show the same increase in noise with particle image size beyond 2 pixels. Having a r_{high} value larger than r_{low} indicates that the distribution is skewed to the high side. Note that these uncertainty values are very small.

The uncertainties stemming from displacement are also small as shown in Fig. 4.12. The random distribution is skewed toward the low side for smaller displacements, but switches to the high side for displacements larger than 0.5 pixels. Raffel's results did not employ window shifting, which is the reason for the non-periodic behavior of the uncertainty. The PRANA displacement uncertainties as a function of displacement are similar (accounting for the factor of 1.96 difference between the definition of ϵ_{rms} and r), and are periodic. These results are not shown, but like Raffel's result, increasing particle density decreases the fluctuations. This is likely due to increased correlation strength for increased particles. Also, the bias uncertainty grows with increasing particle density. For the low density shown,

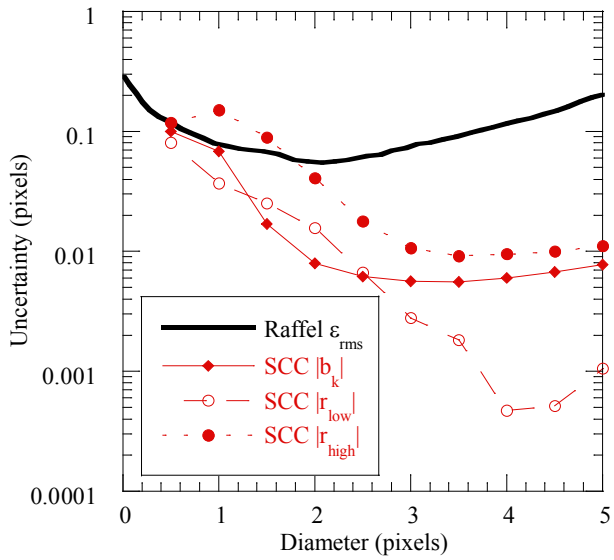

Fig. 4.11: A comparison between the rms uncertainty reported by Raffel and the bias, upper random and lower random uncertainty from this study due to particle image diameter. The SCC method is used with interrogation regions of 16×16 pixels with $N_I = 5$. All images have 8 bit resolution, no noise, and particle image diameters of 2.0 pixels.

the bias is very small.

The uncertainties due to shear are much larger for any PIV code compared to uniform displacements . Figure 4.13 shows that even small amounts of shear dramatically increase the uncertainty, while the floor uncertainty for Raffel's result is larger. Both algorithms improved with seeding density in a similar manner.

4.5 Image Parameter Quantification

To use these uncertainty estimates, image parameters need to be quantified for non-synthetic data. The easiest parameter to quantify is displacement since the PIV algorithm already calculates this. Since it is the value of the subpixel displacement that creates error (assuming it is not a spurious vector), this quantity is stored for each vector. Depending on the algorithm used, this value can be determined by multiplying the velocity by Δt, then rounding the displacement to the neared integer pixel value, and taking the difference from

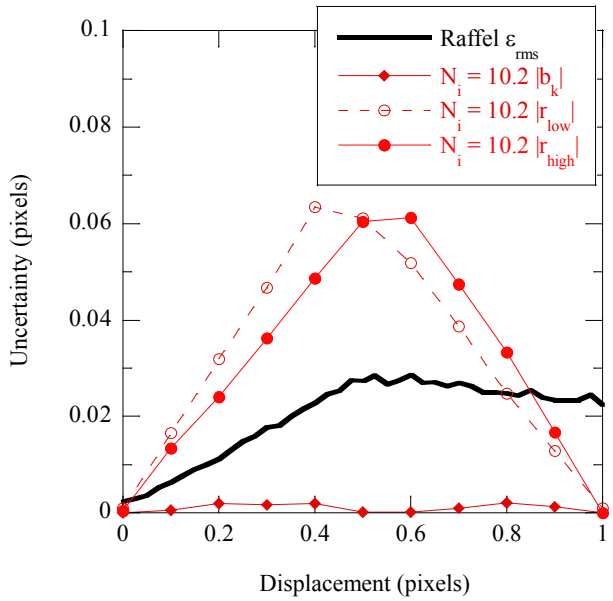

Fig. 4.12: A comparison between the rms uncertainty reported by Raffel and the bias, upper random and lower random uncertainty from this study due to displacement. The SCC method is used with interrogation regions of 32×32 pixels with $N_I = 10.2$. All images have 8 bit resolution, no noise, and particle image diameters of 2.2 pixels.

the unrounded value.

The average particle image diameter and the average density are not as straight forward to determine. A preliminary method to automatically estimate the particle image diameter and density has been developed. Rows (or columns) of pixel intensities are selected from each PIV image pair. Each row is then averaged with the preceding and following rows. A plot of this is shown in Fig. 4.14. Because real images will have background noise, a threshold value must be set such that background noise has a minimal impact on the diameter estimate. The peaks that extend above the threshold level are assumed to represent a particle image or cluster of multiple particle images. Peaks corresponding to multiple particle image clusters will be generally larger in magnitude and wider than those of single particle images. A gaussian curve is then fit to each peak above the threshold. The standard deviation, s_x, of the gaussian curve is computed for each assumed particle. The particle diameter is then estimated to be $2(1.6)(s_x)$, where the value 1.6 was empirically determined. An average

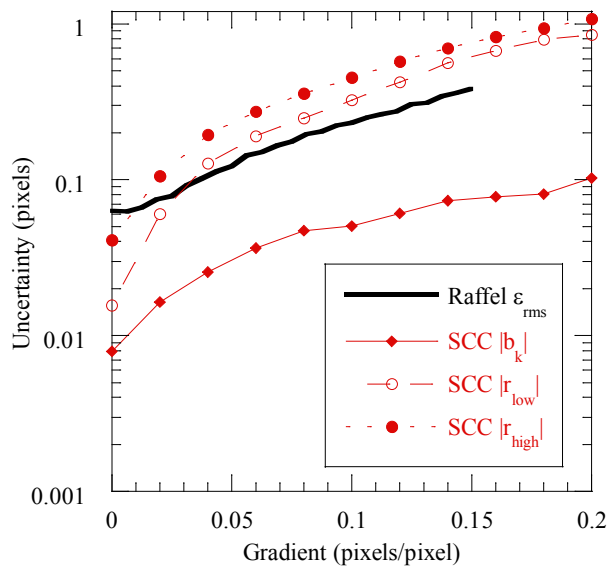

Fig. 4.13: A comparison between the rms uncertainty reported by Raffel and the bias, upper random and lower random uncertainty from this study due to shear. The SCC method is used with interrogation regions of 16×16 pixels with $N_I = 5$. All images have 8 bit resolution, no noise, and particle image diameters of 2.0 pixels.

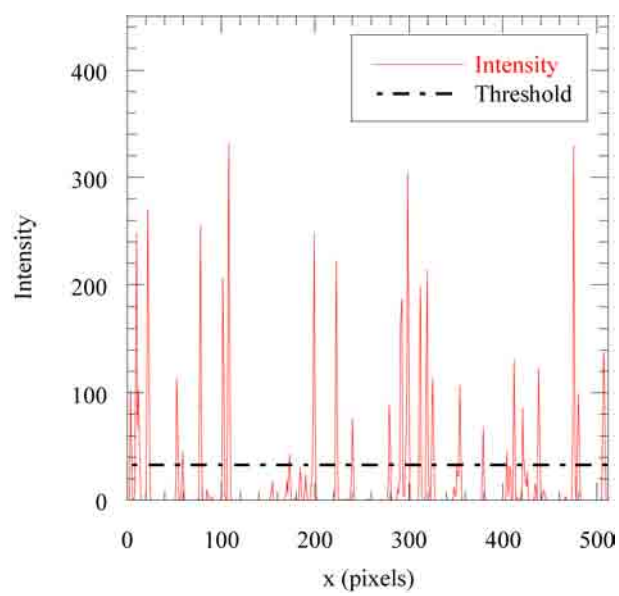

Fig. 4.14: A singe row added to the preceding and following rows of pixel intensity. Based on this singe row the algorithm computed the particle image diameter such that the relative error $[\mathrm{abs}(\mathrm{d}_{\tau\mathrm{true}} - \mathrm{d}_{\tau})/\mathrm{d}_{\tau\mathrm{true}}]100\% = 3.7\%$. The particle image density relative error was computed the same way to be 8.8%.

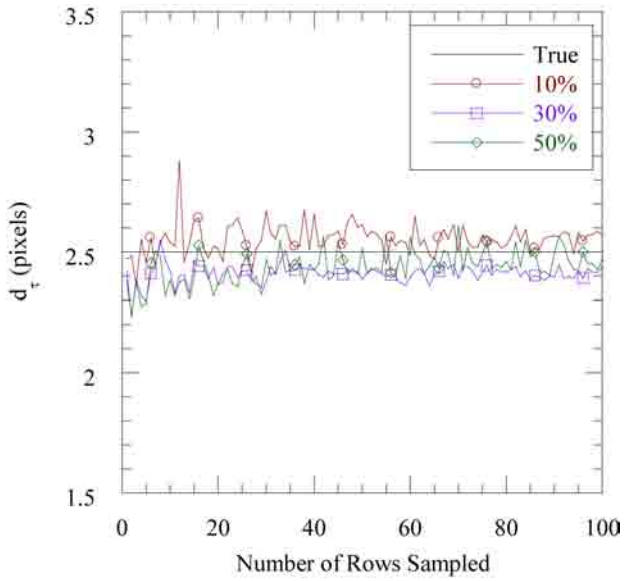

Fig. 4.15: Particle image diameter, d_τ, is estimated with varying number of rows sampled. The noise threshold is set to 10%, 30%, and 50% of the maximum intensity.

particle image diameter is then found from all the gaussian fits. Other methods such as those used in Particle Tracking Velocimetry measurements may be used.

Using the gaussian fit for each assumed particle reduces the effect that the selected noise threshold has on the estimated d_τ which is seen in Fig. 4.15. It is also seen that an average particle image predicted after sampling 30 rows becomes fairly constant. The exact values of each estimated particle image diameter varies randomly about a mean value. This is due to the random distribution of particles within each image. This scheme produces a very accurate estimate of the particle diameter for particles larger than 1 pixel, as shown in Fig. 4.16.

As a first approximation of the background noise for an image, the threshold is set to the sum of the average pixel intensity of the image, $\bar{x}$, and the standard deviation of the pixel intensities s_x. To estimate the particle image density the image intensity values are filtered such that only pixel intensities larger than the threshold remain. The number of particles in the image is then estimated as the number of pixels in the filtered image divided

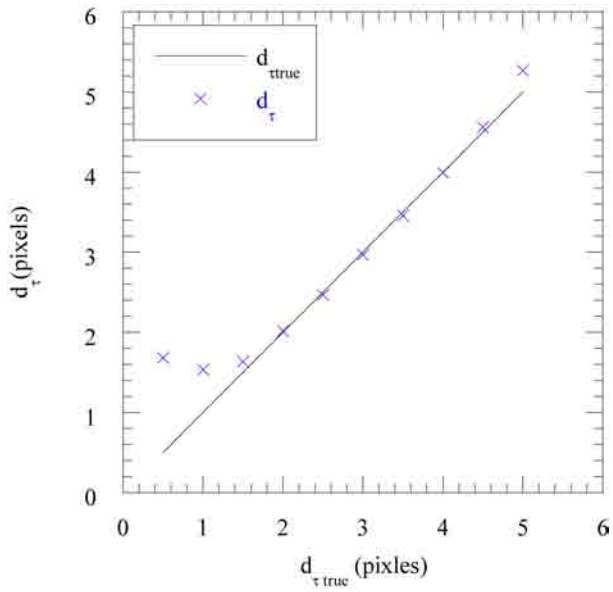

Fig. 4.16: Particle image size algorithm results as a function of particle size.

by the projected area of a particle, which is approximated by that of a circle

$$A_p = \frac{\pi \left(d_\tau\right)^2}{4}. \tag{4.22}$$

The particle density can then be estimated by dividing the number of particles by the pixel area of the image. Experimental results indicate that this method tends to underestimate the particle image density. A correction factor of 1.32 is multiplied to the estimated particle image density estimate to provide a better estimate.

The fourth parameter that is needed for the uncertainty estimate is the velocity gradient. The method used to estimate the velocity gradient is the Robust Gradient Estimate Method described in [29] which has shown improvement in derivative estimates over other methods such as finite difference.

Effects of Noise on Parameter Quantification

The effects of noise on gradient estimation can be found in [29], and the effects of noise on displacement estimation can be found in [19–21]. To see the effects of noise on particle image diameter and density, three levels of background noise are investigated which are

created from a normal distribution with zero mean and variance equal to 0%, 10%, and 20% of the maximum intensity value. Sample images corresponding to these noise levels are seen in Fig. 4.17. A plot of the estimated diameter and density for the three noise levels is seen in Fig. 4.18 and Fig. 4.19. The uncertainty bars on the data points are based on a Student's t distribution with sample size of 4. As we can see the estimate of the particle image diameter remains accurate for the three levels of noise while the estimated particle image density rises with increased noise. The estimation of particle image density will be an area of future study.

From Fig. 4.9 and Fig. 4.10 it is concluded that the accuracy with which this method finds the particle image diameter and density will have little effect on the uncertainty estimate. The ability to accurately predict the uncertainty is most directly related to the accuracy with which the gradient can be estimated.

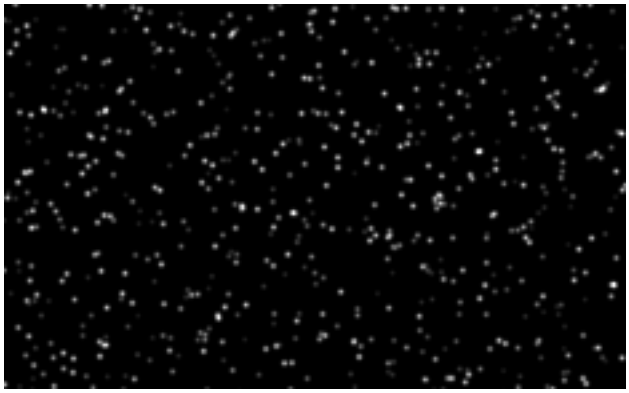

(a)

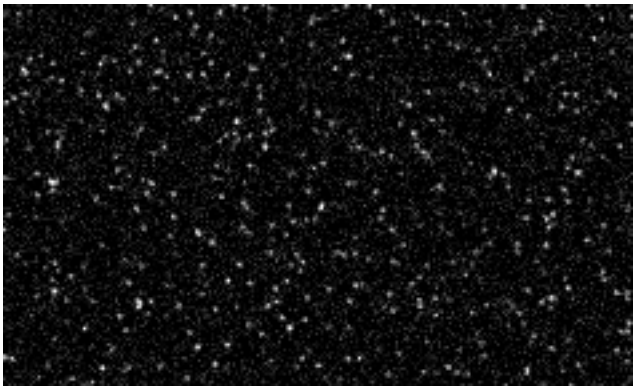

(b)

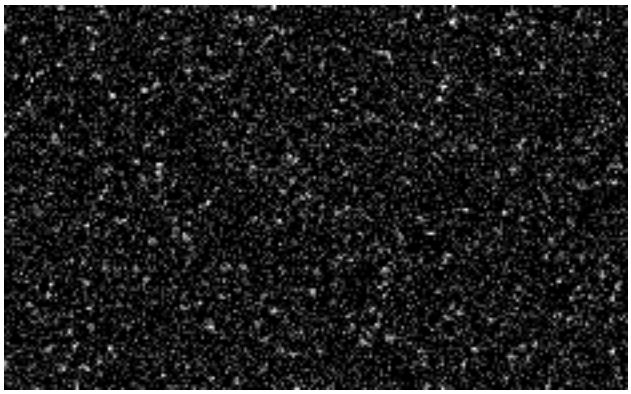

(c)

Fig. 4.17: A section of an image with particle image diameters of 2.5 pixels, density 0.0192 particles/pixel^2 and (a) 0.0% background noise, (b) 10.0% background noise, (c) and 20.0% background noise.

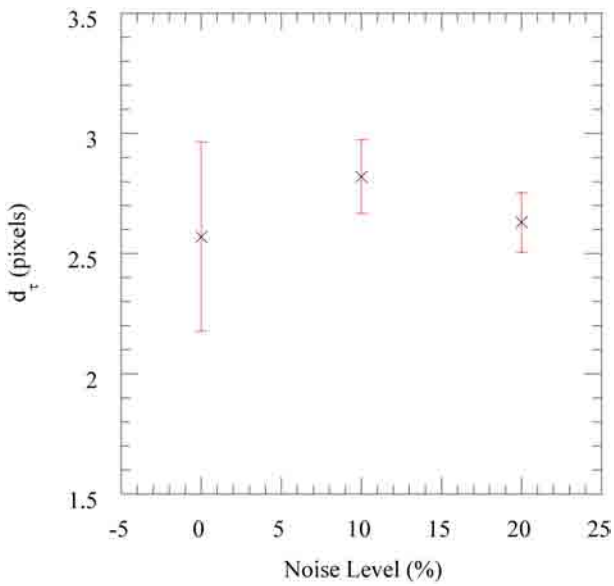

Fig. 4.18: The effect of image background noise on the estimated particle image diameter. The actual value is 2.5 pixels. Uncertainty band width is computed from a Student's t distribution of 4 samples and a 95% confidence interval.

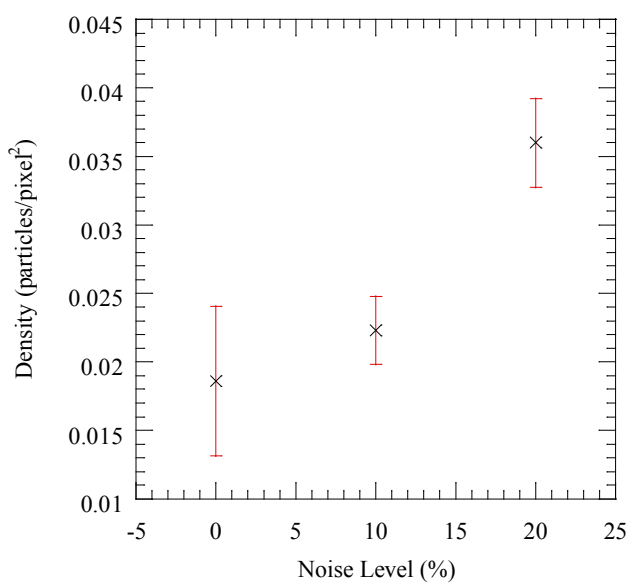

Fig. 4.19: The effect of image background noise on the estimated particle image density. The actual value is 0.02. Uncertainty band width is computed from a Student's t distribution of 4 samples a 95% confidence interval.

Chapter 5

Results

The estimated uncertainty based on the uncertainty surface was computed from flows having a uniform profile, a linear profile, a Couette-Poiseuille flow, a Burger's Vortex, and a laminar separation bubble [25]. Information on how these were generated can be found in chapter 4. Given the synthetic images based on "known" flows, it is possible to determine how often the "true" value lies within the uncertainty bands. Note that the Liner Profile, and Couette-Poiseuille flow have zero mean in the cross stream direction ($v = 0$).

5.1 Assessing the Appropriateness of the Uncertainty Band

The appropriateness of the estimated uncertainty is determined by examining the percentage of calculated vectors which contain the true value within their error bounds. If all error sources have been taken into account, the uncertainty bands on 95% of the computed vectors should contain the true value. This percentage will be refereed to as the "Uncertainty Effectiveness." The uncertainty effectiveness is computed for all flows and three background noise levels (for cases for which images were generated) including no noise, and noise levels corresponding to two common cameras. Differing levels of background noise are included to test the results of [1], that it is negligible, and to make the synthetic images more realistic. The results are tabulated in Table 5.1 for both the standard cross correlation (SCC) and robust phase correlation (RPC) methods. The same inputs to PRANA were used as when the uncertainty surface was generated and can be found in Table 4.2. Note that the PIV Challenger 2005 case B was not processed with noise added, because the images were given for the challenge, not produced for this study.

Each flow analyzed contained $16,129$ vectors with the exception of the PIV Challenge 2005 case B which has 3608 vectors. Each image was post-processed using a median filter

Table 5.1: Uncertainty Effectiveness ($u - U_r^- < u_{true} < u + U_r^+$) for Both the u and v Velocity Components

Flow Type and Correlation	no noise (u/v)	PCO Sensicam QE noise (u/v)	FastCam noise (u/v)
Uniform Flow SCC	78.0% / 66.4%	61.5% / 56.7%	71.0% / 61.9%
RPC	94.1% / 87.9%	89.6% / 83.0%	87.3% / 77.0%
Linear Profile SCC	93.0% / 44.5%	92.8% / 44.7%	93.0% / 41.0%
RPC	95.5% / 41.8%	96.1% / 42.7%	95.6% / 39.4%
Couette-Poiseuille SCC	93.3% / 42.8%	92.5% / 45.1%	92.8% / 39.6%
RPC	95.9% / 44.5%	97.4% / 49.6%	95.8% / 41.4%
Burger's Vortex SCC	78.5% / 77.4%	78.4% / 77.5%	78.1% / 77.0%
RPC	86.2% / 83.5%	88.2% / 85.4%	86.0% / 83.1%
PIV Challenge 2005 case B SCC	72.3% / 33.6%	- / -	- / -
RPC	89.9% / 69.0%	- / -	- / -

to remove spurious vectors. In all cases, no more than 0.6% of the vectors were removed by the median filter.

Table 5.1 shows that background noise plays an insignificant role for these flow cases. Also, noise in the raw data can be mitigated through image pre-processing if the levels are significantly high relative to the particle intensities. Numbers significantly lower than 95% indicate that either 1) an error source parameter, such as shear, has been estimated incorrectly or 2) an error source has been neglected.

5.2 Uncertainty Field Computations Compared with Error

The first flow analyzed is that of a uniform velocity field. The data was created with particle image diameters equal to 2.5 pixels, and a particle image density of 0.0293 particles/pixel^2. This case serves as a base line of a simple flow with two significant velocity components and no gradient. The uniform displacement is set such that there is a 3.268 pixel displacement along the x-axis, and a 5.876 pixel displacement along the y-axis. A plot of the velocity field and the computed width of the uncertainty bars, $\sqrt{\left(U_{r_x}^-\right)^2 + \left(U_{r_y}^-\right)^2} + \sqrt{\left(U_{r_x}^+\right)^2 + \left(U_{r_y}^+\right)^2}$, is shown in Fig. 5.1. Figure 5.2 shows that the uncertainty levels are generally small for a flow with zero gradient but that regions of larger

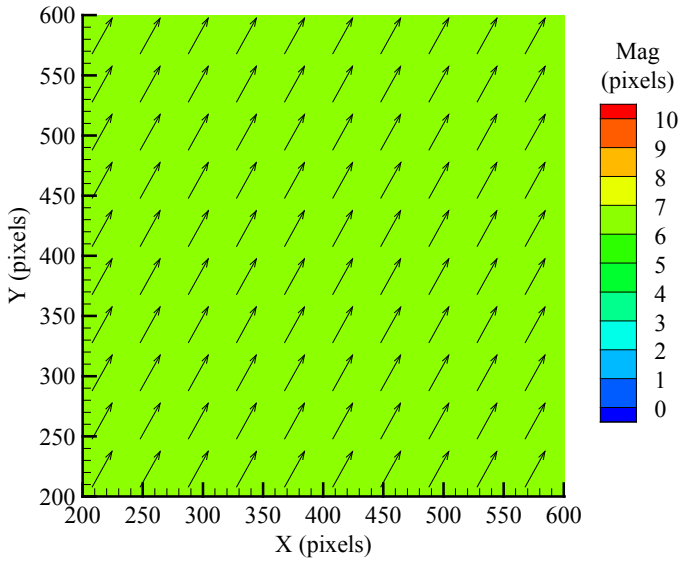

Fig. 5.1: Plot of the calculated displacement of the uniform profile velocity field with no background noise computed with the RPC method.

uncertainty do exist due to other factors. It is also clear that these regions, in most cases, correspond to regions of larger error. This is the desired performance of the method.

For a linear velocity profile (constant gradient of 0.02 pixels/pixel) with particle image diameter equal to 2.5 pixels and particle image density of 0.0293 particls/pixel^2, the velocity field and the width of the uncertainty bars are shown in Fig. 5.3 and 5.4. The majority of the uncertainty bars have the same size, since shear will dominate the uncertainty estimate. The fluctuations in the uncertainty bar width are most likely due to errors in the estimate of the velocity gradients $\partial u/\partial y$ and $\partial v/\partial x$. An error in the computed velocity vector will be amplified during numerical differentiation. Again, however, note the strong correlation between regions of large uncertainty and regions of large error.

Combined Couette-Poiseuille flow, which has a varying gradient, is also analyzed with a particle image diameter equal to 2.5 pixels and a particle image density of 0.0293 particls/pixel^2. The velocity field and the width of the uncertainty bars are shown in Fig. 5.5 and 5.6. As expected, the width of uncertainty bars increased in areas of higher shear and decrease in areas of low shear when the uncertainty due to displacement becomes significant. A plot

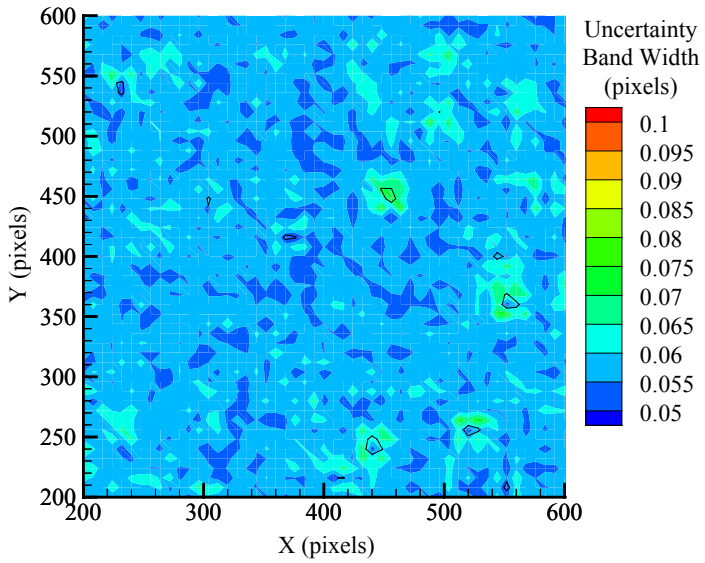

Fig. 5.2: Plot of the width of the uncertainty bar associated with each displacement vector and superimposed error contour for the uniform flow case. The error level contours are 0.0, 0.05, and 0.1 pixels.

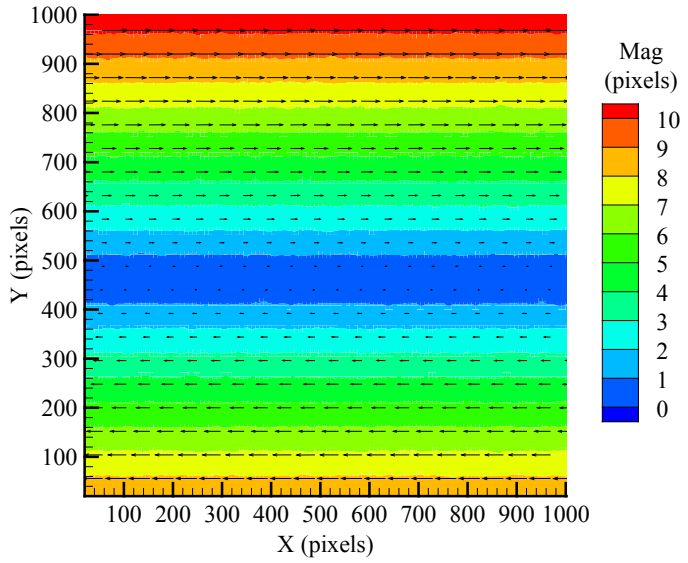

Fig. 5.3: Plot of the calculated displacement of the linear profile velocity field with no background noise as computed with the RPC method.

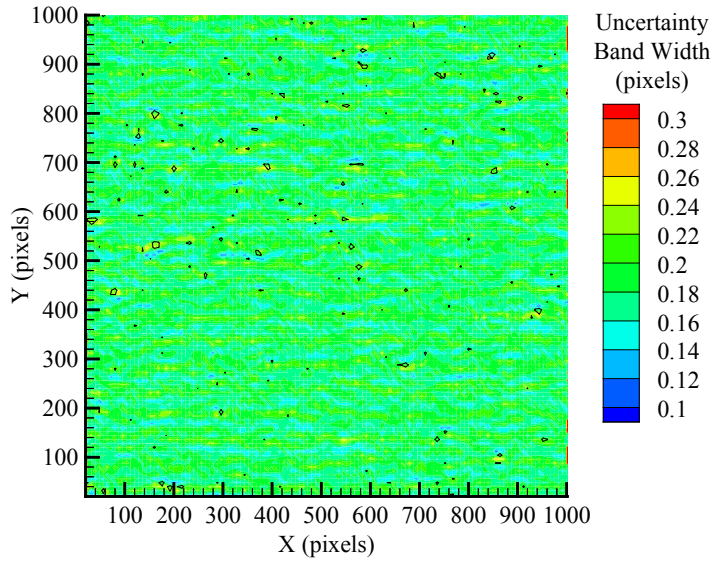

Fig. 5.4: Plot of the width of the uncertainty bar associated with each displacement vector and superimposed error contour for the linear profile case. The error level contours are set at 0.0, 0.1, and 0.2 pixels.

showing the u velocity profile is shown in Fig. 5.7 with 95% confidence uncertainty bars and the true value of u.

A Burger's Vortex, which is a rotating flow, is also analyzed. The particle image diameter is 2.5 pixels, and particle image density is 0.0195 particls/pixel^2. A plot of the velocity field, and the computed width of the uncertainty bars are shown in Fig. 5.8 and 5.9. The gradients ($\partial u/\partial y$ and $\partial v/\partial x$) in this flow are small and constant. Because of the small gradients, the uncertainty due to the subpixel displacement, which is sinusoidal, is significant.

For the PIV Challenge 2005 case B data the major source of error comes from shear, the effects of which dominate the uncertainty estimates. A plot of the velocity field, and the computed width of the uncertainty bars are shown in Fig. 5.10 and 5.11. It is seen that the predicted uncertainty values are higher in areas of larger error.

The importance of individual uncertainty estimates can easily be seen when a plot is made showing the uncertainty bar width as a percentage of the local velocity. This was

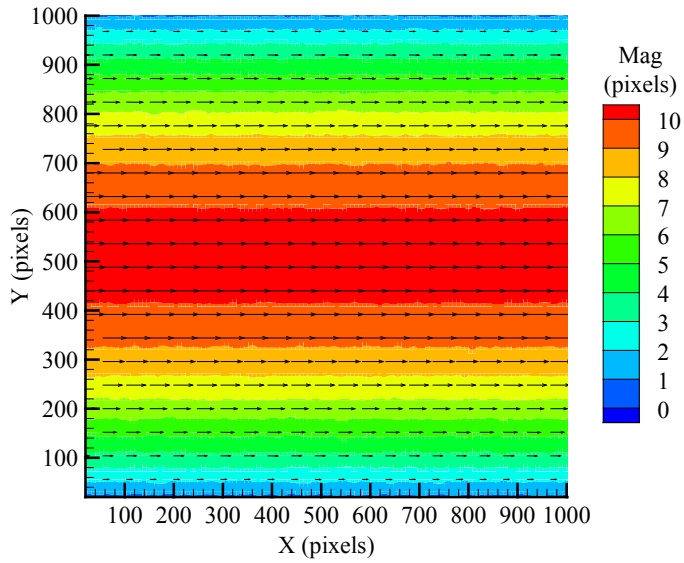

Fig. 5.5: Plot of the calculated Couette-Poiseuille flow field displacement with no background noise as computed by the RPC method.

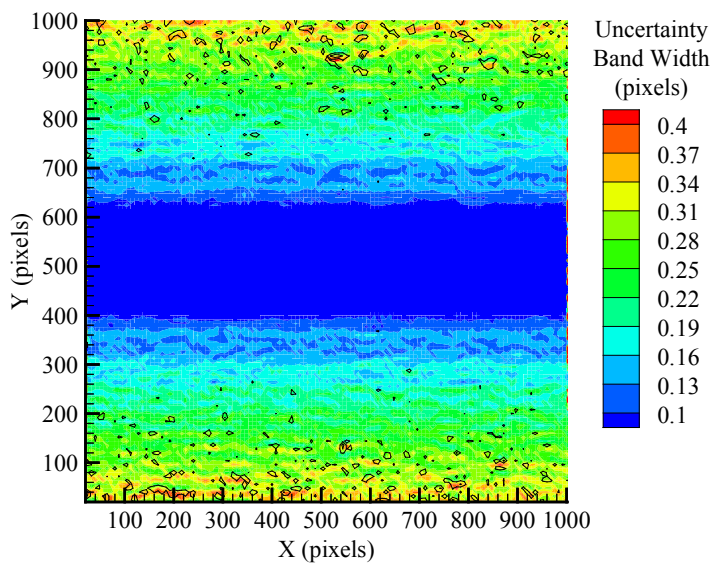

Fig. 5.6: Plot of the width of the uncertainty bar associated with each displacement vector and superimposed error contour for the Couette-Poiseuille flow case. The error level contours are 0.0, 0.1, and 0.2 pixels.

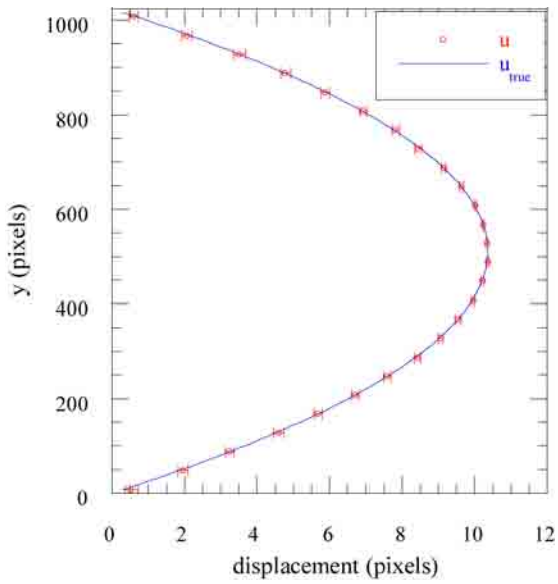

Fig. 5.7: Comparison of the computed value of u and its 95% uncertainty bar at constant $x = 31$mm for a Couette-Poiseuille ow which has 10% background noise.

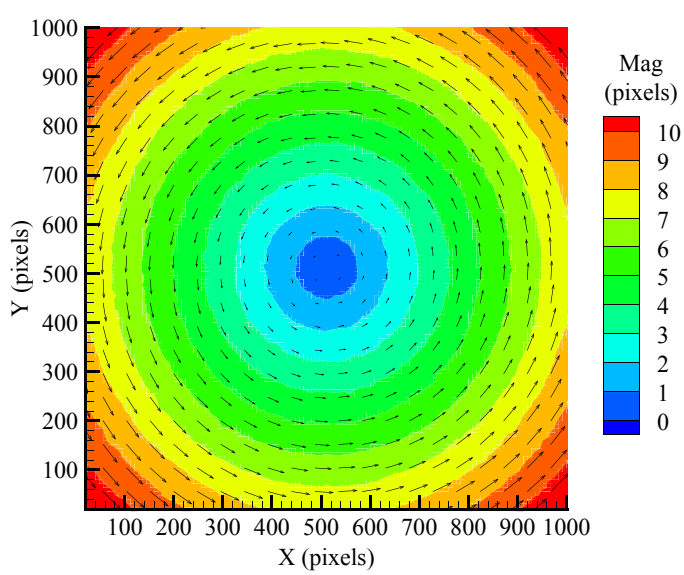

Fig. 5.8: Plot of the calculated Burger s Vortex ow eld displacement with no background noise as computed by the RPC method.

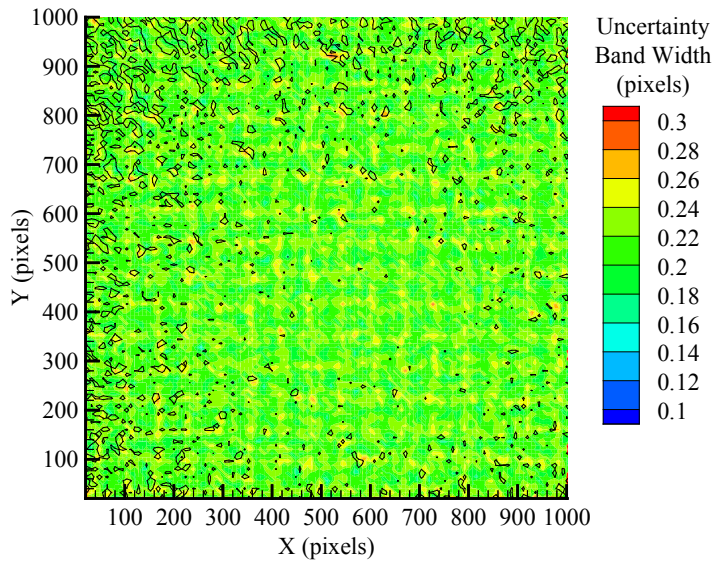

Fig. 5.9: Plot of the width of the uncertainty bar associated with each displacement vector and superimposed error contour for the Burger Vortex case. The error level contours are 0.0, 0.1, and 0.2 pixels.

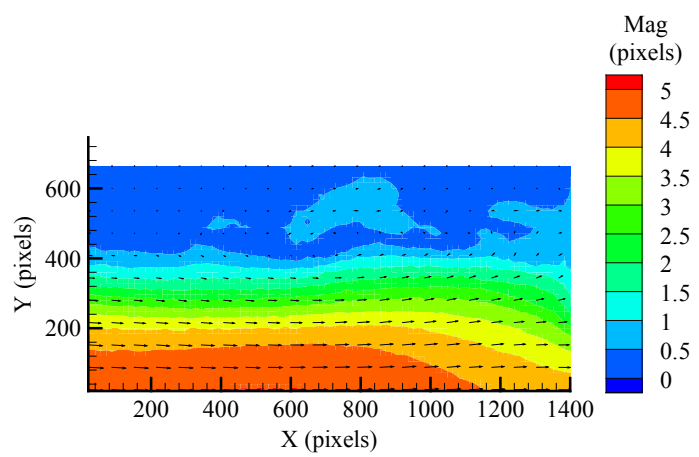

Fig. 5.10: Plot of the PIV Challenge 2005 case B flow field displacement as computed by the RPC method.

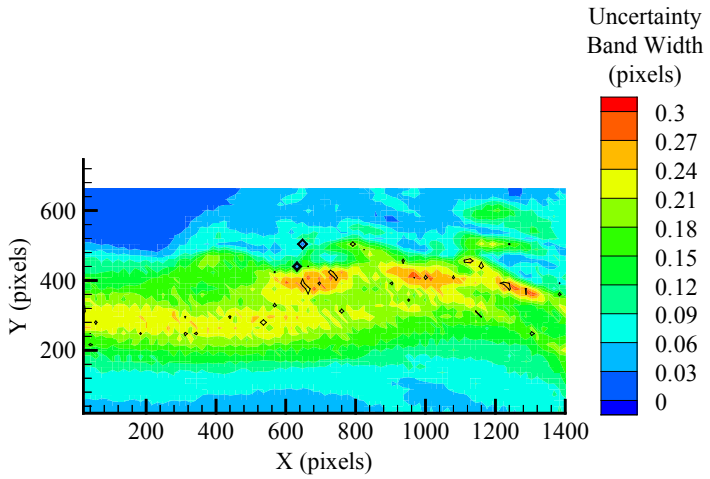

Fig. 5.11: Plot of the width of the uncertainty bar associated with each displacement vector in the DNS flow field with superimposed error contours. The error level contours are set at 0.0, 0.1, 0.2, and 0.3 pixels.

done for the combined Couette-Poiseuille flow (Fig. 5.12) and the PIV Challenge 2005 case B flow (Fig. 5.13). Channel flow is often thought of as having high uncertainty near the wall. Some of this velocity field may have an acceptable level of uncertainty. Using a single uncertainty value for the entire flow (which is common) obscures the fact that some of the data are much better that others.

It is seen in Fig. 5.13 that for a flow which appears to have a reasonable velocity profile (Fig. 5.10), the uncertainty for local velocity values can reach unacceptable levels. If a single uncertainty value were defined for the entire flow region, it would need to be large enough to capture the vectors with the largest uncertainty. Such an approach often would label PIV velocity fields with an uncertainty high enough to cause the case to be discarded. If individual uncertainty values are assigned to each local vector, then each vector can be individually assessed based on its uncertainty level. Since the uncertainty estimates generated do not capture 95% of the true values, the uncertainty estimate as a percentage of local velocity is an underestimation. Because of this Fig. 5.12 and Fig. 5.13

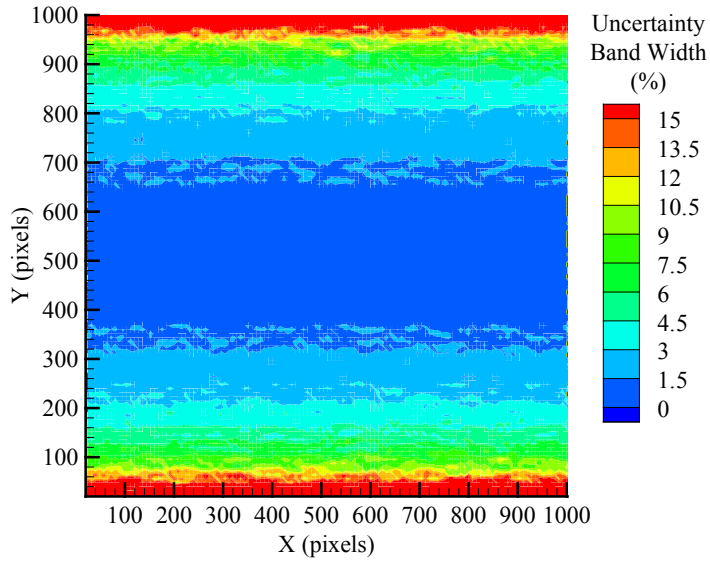

Fig. 5.12: A plot of the local uncertainty estimate as a percentage of local velocity for the combined Couette-Poiseuille flow.

are expected to overestimate the local accuracy of PIV.

5.3 Correction of Uncertainty Estimates

All three cases with small (PIV 2005) or zero (Linear Profile and Couette-Poiseuille) v have very poor coverage for the v component of velocity. Since the two cases with $v = 0$ have inappropriate uncertainty bars on the v components, 1-D flow was further investigated to see if the u and v velocity components within the same interrelation region are correlated with each other. To do this, 50 synthetic image pairs were created with displacements ranging from 0.2 pixels to 10.0 pixels along the x-axis with $v = 0$. Background noise was added to each to approximate that of the PCO CCD camera. Each image pair produced 3969 vectors and was processed according to Table 4.2 Less than 1.5% of vectors were removed in post-processing. Figure 5.14 shows the standard deviation of the y displacement component (which should be zero) for both the SCC and RPC methods.

The periodic behavior appears similar to displacement peak locking. By removing all integer displacements from the data in Fig. 5.14, the same data are shown as a function of

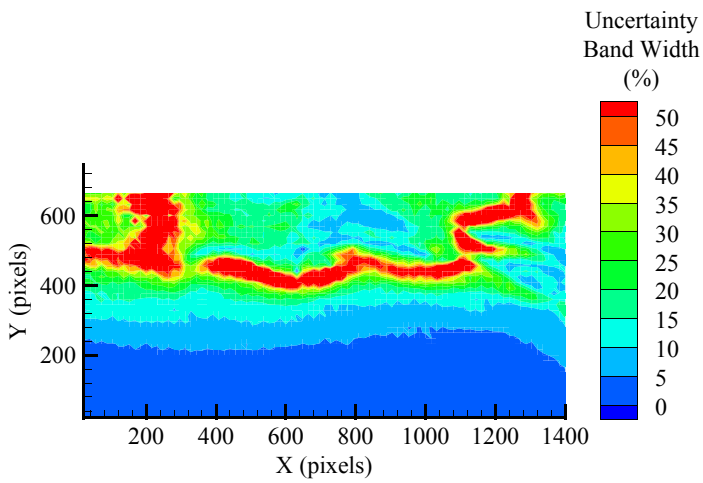

Fig. 5.13: A plot of the local uncertainty estimate as a percentage of local velocity for PIV Challenge 2005 case B ow eld.

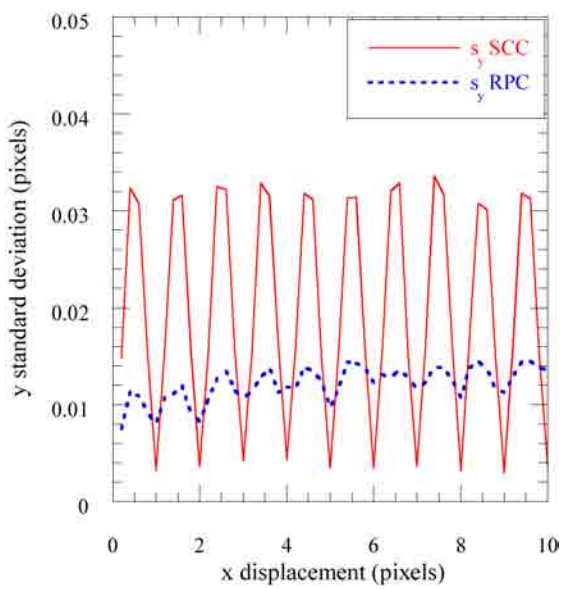

Fig. 5.14: The computed standard deviation of the y velocity component for varying x velocity component particle image displacement for both the standard cross correlation and robust phase correlation methods.

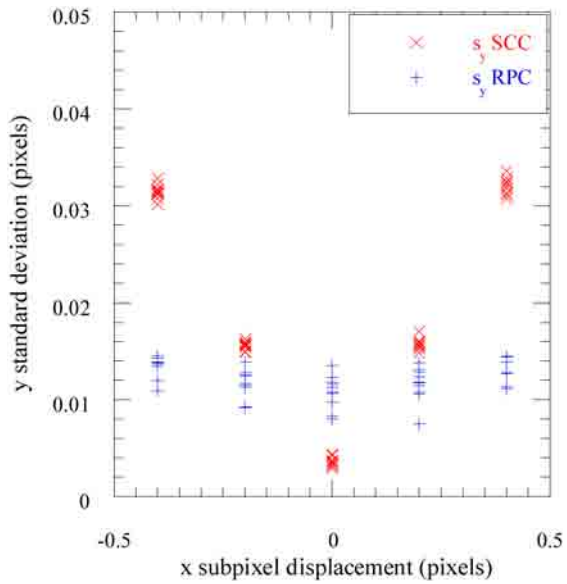

Fig. 5.15: The computed standard deviation of the y velocity component for varying x velocity component particle image subpixel pixel displacements.

subpixel displacement only in Fig. 5.15.

It is apparent that the for the SCC method, there is noise induced on a velocity component proportional to the subpixel displacement on the other component. For the RPC method the amount of noise induced on a velocity component is less than that of the SCC method, but it is still present and actually increases as the displacement of the orthogonal component increases. The uncertainty surface produced for this study did not account for this e ect. This may explain the poor uncertainty estimate on the zero v cases. In fact, this e ect will degrade performance in any case where all other error sources are insigni cant. This also explains why the RPC method, which su ers from this problem to a much smaller extent than the SCC method, provides better uncertainty results than the SCC method even though they each have their own unique uncertainty surface.

5.3.1 Implementation of an Uncertainty Floor

In these cases, the uncertainty is very small and the vector value is close to zero. In these situations, e ects that are not considered in the uncertainty surface can become important, thus leading to poor coverage from the uncertainty bands. The following solution

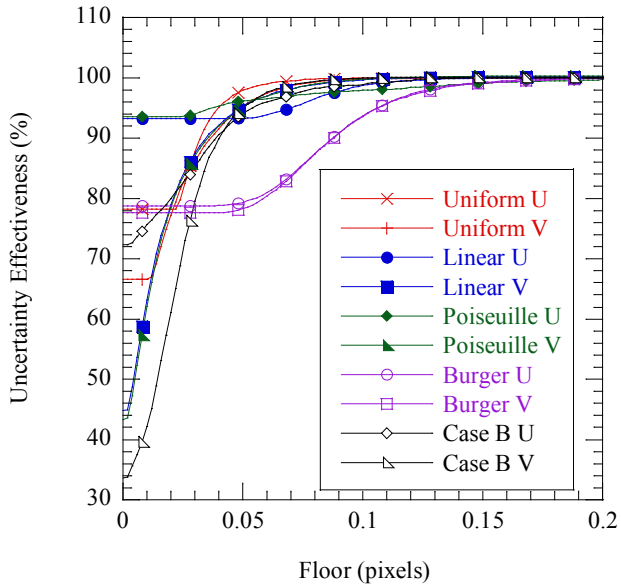

Fig. 5.16: The effects of a floor minimum uncertainty value for the uniform flow, linear profile, Couette-Poiseuille, and Burger's vortex flows when processed with the SCC method.

to this issue: the uncertainty should have a floor or minimum value. Figure 5.16 shows the uncertainty effectiveness as a result of minimum floor value chosen. The floor effects of the RPC method are not shown here as they follow as similar trend. From Fig. 5.16 it is observed that the flow cases, with the exception of the Burger Vortex, reach 95% uncertainty effectiveness with a similar floor value. Based on Fig. 5.16, we have chosen a value of 0.050pixels for the SCC method floor, and 0.023pixels for the RPC method floor. Using this minimum uncertainty value the new results are show in Table 5.2 (background noise cases are not shown as the effect of background noise was shown to be insignificant). These floor values are as expected based on the peak values observed in Fig. 5.15. By comparing Table 5.2 to the original results in Table 5.1 it is seen that the floor provides an adequate correction for all tested flows with the exception of the Burger vortex. The location of uncertainty values which are set to the minimum floor value are confined to areas of the flow which has low, if any shear, and very small displacement. Because of this, we still maintain local uncertainty values, rather than defining a global value. The floor can be though of as the uncertainty level generated by PIV when nothing else significant

Table 5.2: Uncertainty Effectiveness after a Floor of 0.050 Pixels for the SCC Method, and 0.023 Pixels for the RPC Method Was Used

Flow Type and Correlation	Uncertainty Effectiveness (u/v)
Uniform Flow SCC	97.9% / 95.3%
RPC	96.5% / 97.3%
Linear Profile SCC	93.3% / 95.2%
RPC	95.8% / 94.7%
Couette-Poiseuille SCC	96.2% / 95.1%
RPC	96.5% / 92.8%
Burger's Vortex SCC	79.3% / 78.2%
RPC	86.5% / 83.8%
PIV Challenge 2005 case B SCC	94.1% / 94.9%
RPC	93.7% / 90.7%

in the flow is present. It is determined that an important parameter is not accounted for which adds to the uncertainty for the Burger vortex but is not present in the other flows.

5.3.2 Burger Vortex Investigation

In an effort to determine the cause of the underpredicted uncertainty values of the Burger vortex, three Burger vortexes were created which different strengths. From Fig. 5.17 it is seen that the strength, or level of rotation present in the flow effects the uncertainty effectiveness for a given floor value. Figure 5.17 is a good example of what the uncertainty effectiveness will look like when one or more important flow parameters are not accounted for in the local uncertainty estimates. While both the SCC and RPC methods are evaluated, only the SCC results are shown as the RPC results are very similar.

To determine where the true values are not being contained within the uncertainty bounds contours are made showing their location (Fig. 5.18 and 5.19). As expected, these locations also correspond to regions of larger error. The periodic nature of the large error suggests an error source which is periodic. A histogram was used to determine if peak locking might be the cause, or if certain velocity magnitudes are favored over others. It was determined that all velocity magnitudes are effected equally and peak locking is not present in the Burger vortex flows. The correlation surfaces ($C(i, j)$) are also inspected to

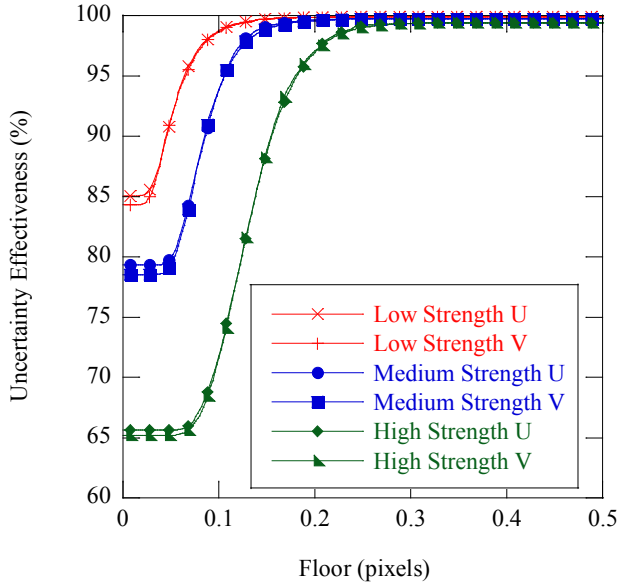

Fig. 5.17: Uncertainty effectiveness shown as a function of the floor value for three Burger vortex cases, each with different strengths.

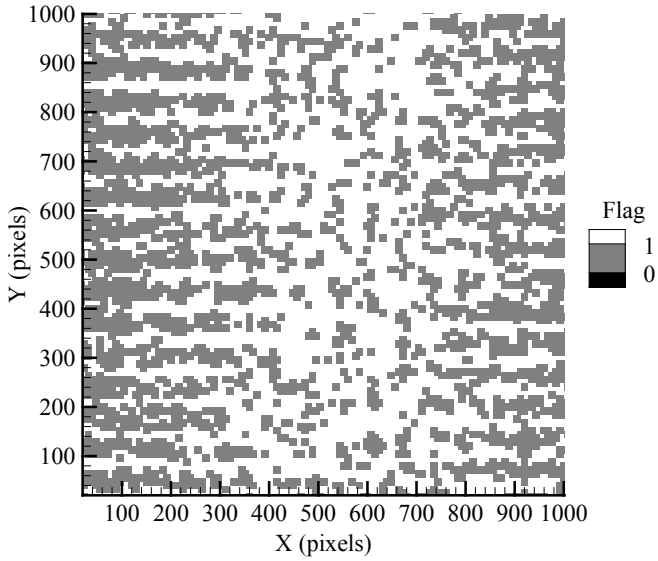

Fig. 5.18: u velocity locations where the true value is not contained within the uncertainty bounds.

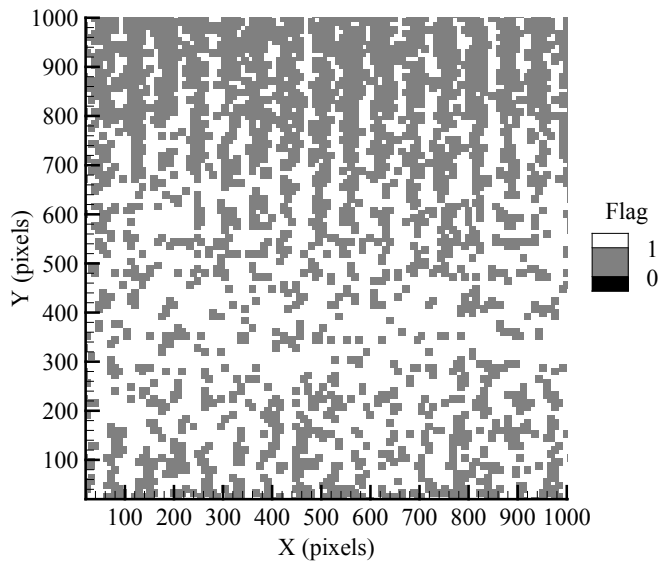

Fig. 5.19: v velocity locations where the true value is not contained within the uncertainty bounds.

determine if something significant was present, and found to appear valid, containing only one large peak similar to Fig. 2.2.

It is proposed that a possible cause of the underprediction uncertainty values is rotation. To determine if rotation is the missing parameter a Rankine vortex is created and tested which contains regions of rotational and irrotational flow. The Rankine vortex velocity is defined as

$$V_\theta = \left| \begin{array}{lll} \omega r & if & r < R \\ \frac{K}{r} & if & r > R \end{array} \right. \tag{5.1}$$

$$V_r = 0 \tag{5.2}$$

where K and ω are constants and R is the radius where the rotation goes to zero [30]. To solve for K and ω such that there is not a discontinuity a maximum velocity is defined as V_{max} and they can be solved for as

$$K = V_{max} R, \tag{5.3}$$

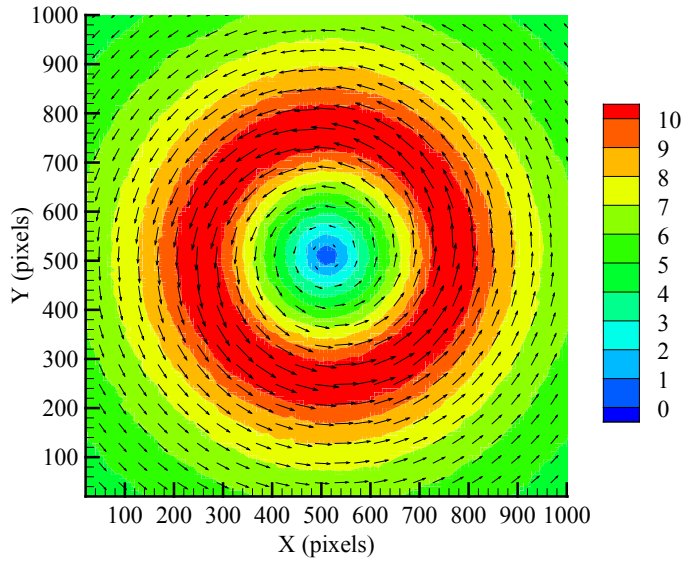

Fig. 5.20: Velocity field of the Rankine vortex.

$$\omega = \frac{V_{max}}{R}. \tag{5.4}$$

Converting to cartesian coordinates is identical to that used when generating the Burger vortex and can be found in Eqn. 4.16. The velocity field is shown in Fig. 5.20 for the Rankine vortex.

The results from the Rankine vortex mimicked those of the Burger vortex. In the Rankine vortex, areas of underpredicted uncertainty which do not contain the true value were found to be periodic, and are prevalent in both the rotational and irrotational regions of the flow. The regions in the Burger vortex which also did not contain the true value within the error bounds are also found to be periodic. Because the uncertainty effectiveness of the Rankine vortex is low in areas of irrotational flow as well as rotational flow it cannot be concluded that rotation is the missing parameter.

To determine the cause of the periodic pattern to the Burger and Rankine vortex underpredicted uncertainties the locations of vectors which did not contain the true value are plotted against the subpixel displacement for that location. Figure 5.21 and 5.22 correspond to the u and v component of the Burger vortex, and Fig. 5.23 and 5.23 correspond to u and

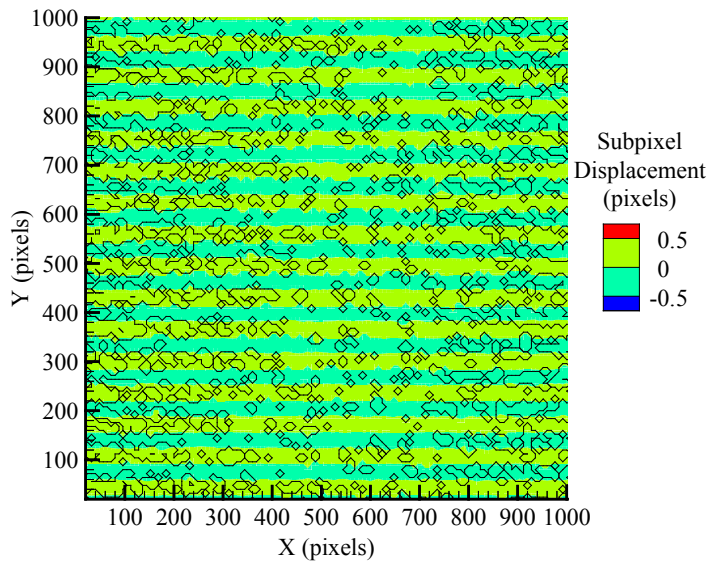

Fig. 5.21: Flood contour of the subpixel displacement estimates for the u velocity component of the Burger vortex case. Line contours are overlaid showing regions where the true value was not captured by computed uncertainty bounds.

v of the Rankine vortex. It is noted that for both the Burger and Rankine vortex that an underpredicted uncertainty is correlated to the velocity subpixel component of displacement and the magnitude of the orthogonal component. For example, where v is large and negative, and the subpixel displacement of u is positive, the uncertainty is underpredicted for u. The reverse of this is also true for the v component.

A second cause is proposed for the underpredicted uncertainty, the displacement of the orthogonal velocity component adds to the uncertainty of the velocity component. A correction factor is desired to scale the predicted uncertainty values based on the orthogonal velocity component magnitude. The correction factor (C_f) scales the uncertainty according to

$$U_{r_{new}} = \sqrt{U_r^2 + (C_f U_r)^2} \tag{5.5}$$

where U_r represents either U_r^+ or U_r^- and $U_{r_{new}}$ is the new uncertainty estimate. To compute C_f additional flow cases are produced. Three flow cases are made which have a constant shear level for the u component (0.02, 0.04, and 0.06pixels/pixel), and the v component

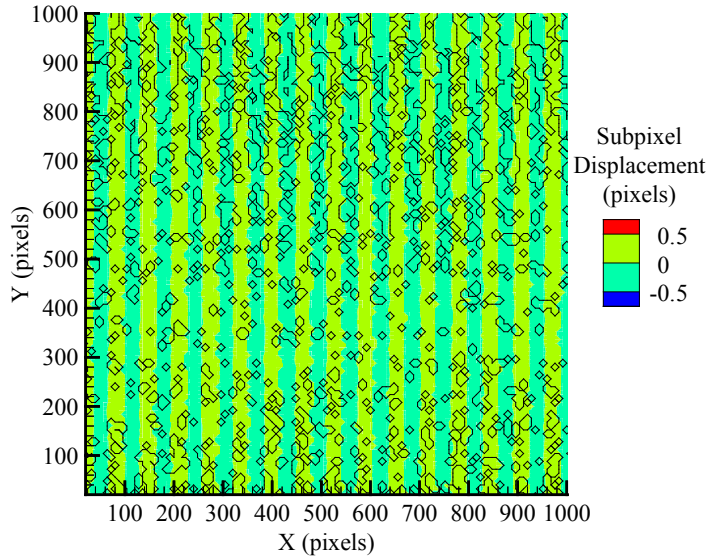

Fig. 5.22: Flood contour of the subpixel displacement estimates for the v velocity component of the Burger vortex case. Line contours are overlaid showing regions where the true value was not captured by computed uncertainty bounds.

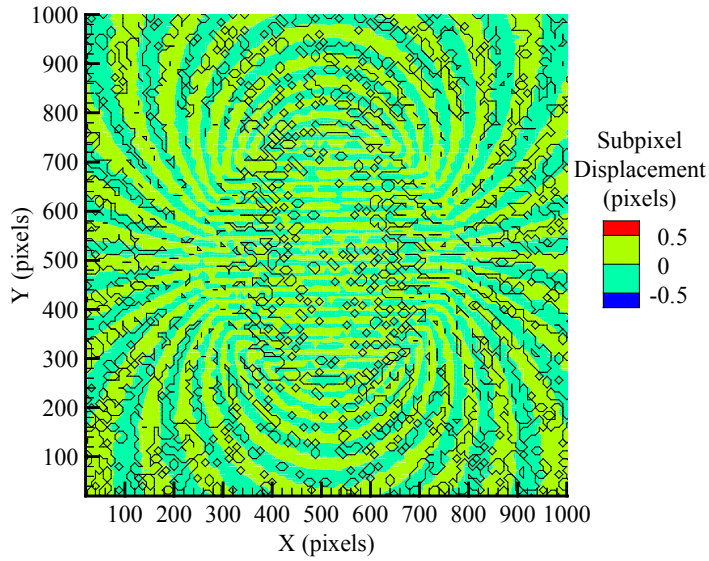

Fig. 5.23: Flood contour of the subpixel displacement estimates for the u velocity component of the Rankine vortex case. Line contours are overlaid showing regions where the true value was not captured by computed uncertainty bounds.

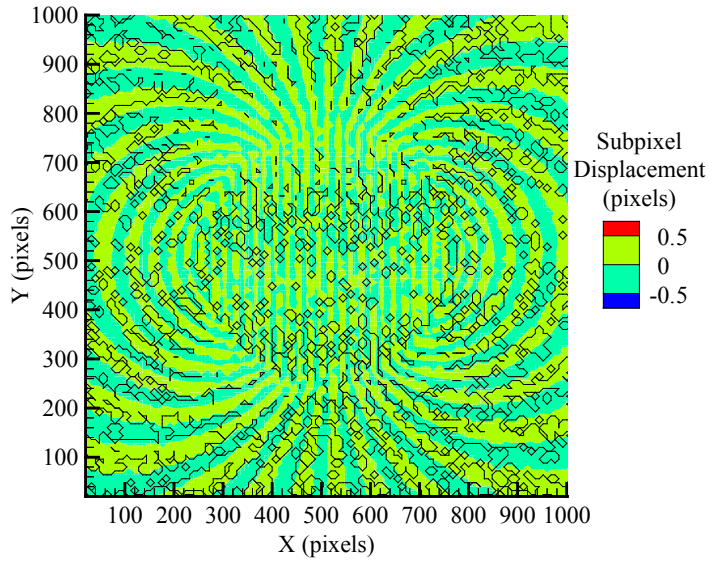

Fig. 5.24: Flood contour of the subpixel displacement estimates for the v velocity component of the Rankine vortex case. Line contours are overlaid showing regions where the true value was not captured by computed uncertainty bounds.

is uniform (varied from $0.00 - 10.75$pixels for each shear level). The shear and orthogonal velocity component magnitudes for the generated flows are comparable to those found in the Burger and Rankine vortex cases. Since the flow fields have uniform shear, and uniform orthogonal velocity component magnitudes a global uncertainty value is assumed sufficient. The global value is defined as the average local predicted uncertainty value. The global value assumption is validated by computing the standard deviation for the mean local value and found to be only a few percent. This is because even though displacement effects uncertainty, the shear will dominate these cases. The uncertainty floor is raised for each case until the uncertainty effectiveness for each case reaches 95%. This floor value is take as the needed uncertainty bound for the flow (U_N). From this value C_f is calculated as

$$C_f = \frac{\sqrt{U_N^2 - U_r^2}}{U_r} \tag{5.6}$$

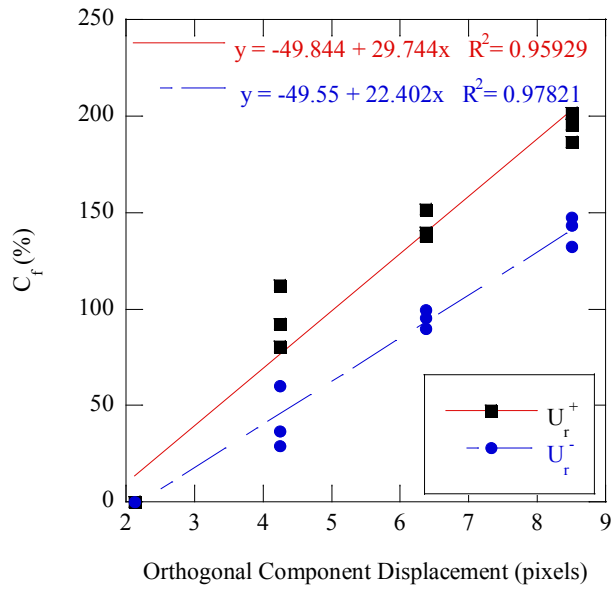

Fig. 5.25: Individual C_f values computed for different shear levels and orthogonal velocity component displacement magnitudes. A linear curve fit is applied to the data which can be used to compute a correction factor for two-dimensional flows.

again, where U_r represents either U_r^+ or U_r^-. The results from the flows is seen in Fig. 5.25. A linear curve fit was used to determine the correction factor as a percent and is

$$C_{f_u} = -49.844 + 29.744v \quad R^2 = 0.95929, \tag{5.7}$$

$$C_{f_v} = -49.55 + 22.402u \quad R^2 = 0.97821. \tag{5.8}$$

It was verified that the predicted uncertainty levels for these flows could be scaled by a correction factor based on the orthogonal component magnitude to bring the uncertainty effectiveness to 95% for all shear cases tested. This correction was then used on the Burger vortex cases. The correction applied to the high strength Burger vortex is shown in Fig. 5.26. From Fig. 5.26 it is shown that while the taking into account the uncertainty increase due to the magnitude of the orthogonal velocity component did increase the uncertainty effectiveness, the 95% desired value is not reached.

It is determined that an additional parameter is needed, or the effect of the orthogonal

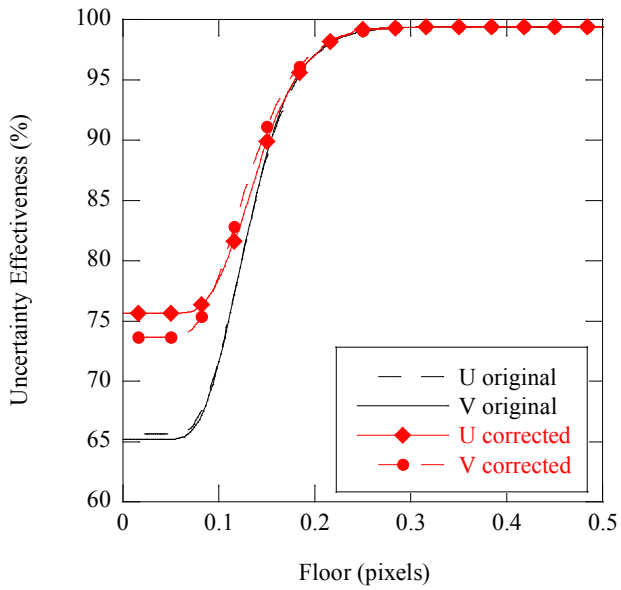

Fig. 5.26: Uncertainty effectiveness shown as a function of the floor value for the high strength Burger vortex case. Both the original results and the corrected results using the uncertainty scaling based on the orthogonal velocity component magnitude are shown.

velocity component on the uncertainty of the desired velocity component is more complex than the magnitude alone. The determination of these effects, both the cause and mechanism, are thus left to a future indepth study. These results were only tested for the specific setting used in PRANA, and it us unknown if they are present in other PIV algorithms.

Chapter 6

Conclusion

A method to compute local PIV velocity vector uncertainty is demonstrated. The method focused on traditionally accepted image parameters which are thought to produce error in PIV measurements, namely: particle image diameter, particle density, particle displacement, and local shear. It is shown that an estimate of the velocity uncertainty can be made for every velocity vector in a flow field. The results shown are specific to the PRANA algorithm, although similar results could be made with other algorithms. The uncertainty estimate is less sensitive to particle image diameter, density, and displacement (with some exceptions) but highly sensitive to shear.

This method tended to grossly under predict the uncertainty levels for one dimensional flows for the component with no displacement. It is suggested that this is because motion in one direction introduces noise in the orthogonal direction. The method generally under predicts the the uncertainty levels for all two dimensional flows analyzed. Motion induced noise is different from dynamic range in that it affects accuracy even when particle displacements are very small or of similar magnitudes. The level of uncertainty caused by the motion induced noise is dependent on the PIV algorithm chosen. Further work is needed to better understand and quantify the effect of motion induced noise.

The importance of local velocity uncertainty estimation has been demonstrated. For flows which have "good" looking velocity fields, the local uncertainty can reach unacceptable levels. With local uncertainty values, areas of the flow can be assessed and removed when uncertainty levels are too high, while other sections of flow may be retained and used. This is a significant improvement over global uncertainty estimates.

While the method presented has flaws that need to be addressed and is probably not yet general enough for wide spread use, the potential and importance of local uncertainty

estimates for PIV has been amply demonstrated.

References

[1] Raffel, M., Willert, C., and Kompenhans, J., *Particle Image Velocimetry*, Springer-Verlag, Berlin Heidelberg, 1998.

[2] Versteeg, H. K. and Malalasekera, W., *An Introduction to Computational Fluid Dynamics the Finite Volume Method*, Pearson, Edinburgh Scotland, 2007.

[3] Westerweel, J., "Fundamentals of Digital Particle Image Velocimetry," *Measurement Science and Technology*, Vol. 8, 1997, pp. 1379–1392.

[4] Keane, R. D. and Adrian, R. J., "Optimization of Particle Image Velocimeters. Part I: Double Pulsed Systems," *Measurement and Science Technology*, Vol. 1, 1990, pp. 1202–1215.

[5] Westerweel, J., *Digital Particle Image Velocimetry: Therory and Application*, PhD Thesis, Delft University of Technology, Delft, Netherlands, 1993.

[6] Bolinder, J., "On the Accuracy of a Digital Particle Image Velocimetry System," ISSN 0282-1990, Lund Institute of Technology, June 1999.

[7] Roth, G. I. and Katz, J., "Five Techniques for Increasing the Speed and Accuracy of PIV Interrogation," *Measurement Science and Technology*, Vol. 12, 2001, pp. 238–245.

[8] James, J. F., *A Student's Guide to Fourier Transforms*, Cambridge University Press, New York, NY, 2002.

[9] Scarano, F., "Theory of Non-Isotropic Spatial Resolution in PIV," *Experiments in Fluids*, Vol. 35, 2003, pp. 268–277.

[10] Westerweel, J., Dabiri, D., and Gharib, M., "The Effect of a Discrete Window Offset on the Accuracy of Cross-Correlation Analysis of Digital PIV Recordings," *Experiments in Fluids*, Vol. 23, 1997, pp. 20–28.

[11] Kim, B. J. and Sung, H. J., "A Further Assessment of Interpolation Schemes for Window Deformation in PIV," *Experiments in Fluids*, Vol. 41, 2006, pp. 499–511.

[12] Scarano, F., "Iterative Image Deformation Methods in PIV," *Measurement Science and Technology*, Vol. 13, 2002, pp. R1–R19.

[13] Gui, L., Merzkirch, W., and Fei, R., "A Digital Mask Technique for Reducing the Bias Error of the Correlation-Based PIV Interrogation Algoritm," *Experiments in Fluids*, Vol. 29, 2000, pp. 30–35.

[14] Huang, H., Dabiri, D., and Gharib, M., "On Errors of Digital Particle Image Velocimetry," *Measurement and Science Technology*, Vol. 8, 1997, pp. 1427–1440.

[15] Westerweel, J., "Efficient Detection of Spurious Vectors in Particle Image Velocimetry Data," *Experiments in Fluids*, Vol. 16, 1994, pp. 236–247.

[16] Fincham, A. M. and Spedding, G. R., "Low Cost, High Resolution DPIV for Measurment of Turbulent Fluid Flow," *Experiments in Fluids*, Vol. 23, 1997, pp. 449–462.

[17] Fincham, A. M. and Delerce, G., "Advanced Optimization of Correlation Imaging Velocimetry Algoritms," *Experiments in Fluids*, Vol. Suppl., 2000, pp. S13–S22.

[18] Carr, Z. R., Ahmed, K. A., and Forliti, D. J., "Spatially Correlated Precision Error in Digital Particle Image Velocimetry Measurements of Turbulent Flows," *Experiments in Fluids*, Vol. 47, 2009, pp. 95–160.

[19] Eckstein, A. C., Charonko, J., and Vlachos, P., "Phase Correlation Processing for DPIV Measurements," *Experiments in Fluids*, Vol. 45, 2008, pp. 485–500.

[20] Eckstein, A. and Vlachos, P., "Assessment of Advanced Windowing Techniques for Digital Particle Image Velocimetry (DPIV)," *Measurement Science and Technology*, Vol. 20, 2009, pp. 075402.

[21] Eckstein, A. C. and Vlachos, P. P., "Digital Particle Image Velocimetry (DPIV) Robust Phase Correlation," *Measurement Science and Technology*, Vol. 20, 2009, pp. 055401.

[22] Coleman, H. W. and Steele, W. G., *Experimentation, Validation, and Uncertainty Analysis for Engineers*, John Wiley and Sons, Hoboken, NJ, 3rd ed., 2009.

[23] Stanislas, M., Okamoto, K., and Kaehler, C., "Main Results of the First International PIV Challenge," *Measurement Science and Technology*, Vol. 14, 2003, pp. R63–R89.

[24] Stanislas, M., Okamoto, K., Kahler, C. J., and Westerweel, J., "Main Results of the Second International PIV Challenge," *Experiments in Fluids*, Vol. 39, No. 2, 2005, pp. 170–191.

[25] Stanislas, M., Okamoto, K., Kaehler, C. J., Westerweel, J., and Scarano, F., "Main Results of the Third International PIV Challenge," *Experiments in Fluids*, Vol. 45, 2008, pp. 27–71.

[26] White, F., *Viscous Fluid Flow*, McGraw-Hill, New York, NY, 2006.

[27] Ogawa, A., *Vortex Flow*, CRC Press, Boca Raton, FL, 1993.

[28] Westerweel, J. and Scarano, F., "Universal Outlier Detection for PIV Data," *Experiments in Fluids*, Vol. 39, 2005, pp. 1096–1100.

[29] Karri, S., Charonko, J., and Vlachos, P. P., "Robust Wall Gradient Estimation Using Radial Basis Functions and Proper Orthogonal Decomposition (POD) for Particle Image Velocimetry (PIV) Measured Fields," *Measurement Science and Technology*, Vol. 20, 2009, pp. 1–14.

[30] Cengel, Y. A. and Cimbala, J. M., *Fluid Mechanics, Fundamentals and Applications*, McGraw Hill, New York, NY, 1st ed., 2006.